Chinese Journal of Natural Medicines

Self-assembled nanoaggregates in Wuzhuyu decoction: formation, absorption, transport, and alleviation of chronic migraine

Qi Wang, Xiaomeng Guo, Meijing Li, Nan Nan, Zekuan Zhang, Zhimin Song, Ziwei Zhou, Nan Zhang, Rui He, Jing Li, Hui Zhao, Renhui Liu, Miao Qu, Muxin Gong

Citation: Qi Wang, Xiaomeng Guo, Meijing Li, Nan Nan, Zekuan Zhang, Zhimin Song, Ziwei Zhou, Nan Zhang, Rui He, Jing Li, Hui Zhao, Renhui Liu, Miao Qu, Muxin Gong, Self-assembled nanoaggregates in Wuzhuyu decoction: formation, absorption, transport, and alleviation of chronic migraine, Chinese Journal of Natural Medicines, 2026, 24(8), 956-971. doi: 10.1016/S1875-5364(26)61201-0.

View online: https://doi.org/10.1016/S1875-5364(26)61201-0

Related articles that may interest you

Shengmaisan combined with Liuwei Dihuang Decoction alleviates chronic intermittent hypoxia-induced cognitive impairment by activating the EPO/EPOR/JAK2 signaling pathway

Chinese Journal of Natural Medicines. 2024, 22(5), 426-440 https://doi.org/10.1016/S1875-5364(24)60640-0

Si-Miao-Yong-An Decoction alleviates thromboangiitis obliterans by regulating miR-548j-5p/IL-17A signaling pathway

Chinese Journal of Natural Medicines. 2024, 22(6), 541-553 https://doi.org/10.1016/S1875-5364(24)60626-6

Protective effects of Wuwei Xiaodu Drink against chronic osteomyelitis through $Foxp3^{+}CD25^{+}CD4^{+}$ Treg cells *via* the IL-2/STAT5 signaling pathway

Chinese Journal of Natural Medicines. 2022, 20(3), 185-193 https://doi.org/10.1016/S1875-5364(22)60146-8

Compound Sophorae Decoction: treating ulcerative colitis by affecting multiple metabolic pathways

Chinese Journal of Natural Medicines. 2021, 19(4), 267-283 https://doi.org/10.1016/S1875-5364(21)60029-8

Effects of Bunao-Fuyuan decoction serum on proliferation and migration of vascular smooth muscle cells in atherosclerotic

Chinese Journal of Natural Medicines. 2021, 19(1), 36-45 https://doi.org/10.1016/S1875-5364(21)60004-3

Effects of *Huatan Jiangzhuo* decoction on diet-induced hyperlipidemia and gene expressions in rats

Chinese Journal of Natural Medicines. 2021, 19(2), 100-111 https://doi.org/10.1016/S1875-5364(21)60011-0

Wechat

Chinese Journal of Natural Medicines 24 (2026) 956-971

Contents lists available at ScienceDirect

Chinese Journal of Natural Medicines

journal homepage: www.cjnmcpu.com/

Original article

Self-assembled nanoaggregates in Wuzhuyu decoction: formation, absorption, transport, and alleviation of chronic migraine

Qi Wang[a,b], Xiaomeng Guo[a,b], Meijing Li[a,b], Nan Nan[c], Zekuan Zhang[a,b], Zhimin Song[a,b], Ziwei Zhou[a,b], Nan Zhang[a,b], Rui He[a,b], Jing Li[a,b], Hui Zhao[a,b], Renhui Liu[a], Miao Qu[d,*], Muxin Gong[a,b,*]

[a] *School of Traditional Chinese Medicine, Capital Medical University, Beijing 100069, China*
[b] *Beijing Key Laboratory of Traditional Chinese Medicine Collateral Disease Theory Research, Beijing 100069, China*
[c] *College of Basic Medical Sciences, Shanxi University of Chinese Medicine, Jinzhong 030619, China*
[d] *Department of Traditional Chinese Medicine, Xuanwu Hospital of Capital Medical University, Beijing 100053, China*

ARTICLE INFO

Article history:
Received 24 November 2025
Revised 15 January 2026
Accepted 5 March 2026
Available online 20 August 2026

Keywords:
Nanoaggregates
Wuzhuyu decoction
Chronic migraine
Self-assemble
Absorption
IL-33/ST2/TRPA1

ABSTRACT

Self-assembled nanoaggregates (SANs) derived from herbal decoctions have emerged as promising natural nanomedicines. However, their formation patterns in multi-herb formulations and therapeutic roles in central nervous system disorders remain unclear. Wuzhuyu decoction (WZYD) is a classical formula for migraine treatment. Here, we reveal that SANs in WZYD (N-WZYDs) are formed through synergistic interactions among multiple herbal ingredients with Euodiae Fructus as the focus. N-WZYDs consisted mainly of proteoglycan scaffolds and small-molecule active components. In chronic migraine (CM) rat models, N-WZYDs significantly alleviated symptoms with efficacy comparable to that of WZYD, potentially *via* inhibition of the IL-33/ST2/TRPA1 signaling pathway. In Caco-2 cells, transport studies indicated that ginsenoside Rg_1, dehydroevodiamine, and rutaevin were poorly absorbed, whereas evodiamine and 6-gingerol were moderately absorbed but significantly active in efflux, indicating the intestine as a key site of action. As an oral medication, intact N-WZYDs accumulated primarily in the intestines and could be internalized by Caco-2 and enterochromaffin cells. Crucially, N-WZYDs promoted serotonin release from enterochromaffin cells more effectively than free active molecules alone and increased peripheral serotonin levels, thereby alleviating CM. By investigating the formation patterns, anti-CM mechanisms, and absorption behaviors of N-WZYDs, this study elucidated their material basis and brain–intestine interactions in treating CM, supporting their further development as therapeutic agents or drug delivery systems.

1. Introduction

Traditional Chinese medicine (TCM) has unique advantages in the treatment of complex diseases because of its multi-component and multi-target characteristics. Decoction, a widely used TCM dosage form, has rapid onset and superior therapeutic effects for various diseases. Studies have shown that heat-induced self-assembled nanoaggregates (SANs) widely exist in decoctions [1], including licorice decoction [2], *Coptis chinensis* decoction [3], Baihu Tang decoction [4], Maxing Shigan Tang decoction [5]. In decoctions, SANs are formed in boiling water through noncovalent interactions of active small molecules such as berberine [6], glycyrrhetinic acid [7], and ginsenoside Rb_1 [8], or through assembly of macromolecules such as polysaccharides [9, 10] and proteins [11, 12]. SANs are becoming more popular compared to single molecules due to their wide availability, simple preparation, and favorable pharmacological activities [13, 14]. Modern research on decoctions has increasingly concentrated on SANs, which generally exhibit well-defined sizes and morphologies, predominantly nanoscale and spherical, and demonstrate superior pharmacological activities. They also have potential for drug-delivery applications, including improving the solubility and stability of active ingredients and promoting their absorption in the gastrointestinal tract [13]. These SANs are capable of withstanding the gastrointestinal environment and are associated with the pharmaceutical activities of decoctions [15], offering a new angle in understanding the mechanism of decoction effects. Nonetheless, systematic studies involving SANs in decoctions, their formation patterns, the correlation between their pharmacological effects and intestinal absorption, are in their infancy and require further investigation.

WZYD is a TCM formula recorded in the *Treatise on Exogenous Febrile Disease* written by Zhongjing Zhang, composed of nearly ripe fruits of *Euodia rutaecarpa* (Euodiae Fructus, WZY), root or rhizome of *Panax ginseng* (Ginseng Radix et Rhizoma, RS), rhizome of *Zingiber officinale* (Zingiberis Rhizoma Recens, SJ), and ripe fruit of *Ziziphus jujuba* (Jujubae Fructus, DZ). WZYD is a representative formula used to treat migraine by dispelling cold and relieving pain. Chronic migraine (CM) evolves from episodic migraine and affects approximately 2.5% of individuals worldwide [16]. It is a complex neurological disorder characterized by

* Corresponding author.
E-mail addresses: qumiao@xwhosp.org (M. Qu); gongmuxin@ccmu.edu.cn (M. Gong)

https://doi.org/10.1016/S1875-5364(26)61201-0
Copyright © 2026, China Pharmaceutical University. Published by Elsevier B.V. All rights are reserved.

headaches occurring on at least 15 days per month for over 3 months, with at least 8 of these days meeting migraine-specific criteria [17, 18]. WZYD has been shown to alleviate hyperalgesia, inhibit migraine chronification and reduce neurogenic inflammation [19-21]. Initial studies indicated that the SANs in WZYD (N-WZYDs) demonstrate significant analgesic effects in an acetic acid-induced pain model in mice, potentially contributing to the analgesic properties of the decoction [22]. However, whether N-WZYDs represent the effective phase state of WZYD for alleviating CM and mediating brain-intestine interactions remains unproven. Therefore, a thorough investigation into the formation patterns, anti-CM therapeutic actions and mechanisms, and absorption behaviors of N-WZYDs is imperative and representative for advancing the modernization of TCM research.

The intestinal tract is the main site for absorption of nutrients and active substances, playing a key role in the bioavailability of oral medications [23]. Serotonin (5-HT) is a key mediator bridging the peripheral and central nervous systems in CM pathogenesis. WZYD has been shown to increase plasma 5-HT levels in CM rats, with elevated 5-HT binding to axonal receptors to indirectly reduce the release of calcitonin gene-related peptide (CGRP), thereby attenuating pain sensitization [19]. As WZYD is administered orally and peripheral 5-HT originates primarily from enterochromaffin (EC) cells, we employed Caco-2 and RIN-14B cells to investigate the intact internalization, absorption behaviors, and 5-HT release-modulating effects of N-WZYDs.

This study integrated TCM with modern nanoscience to elucidate the material basis and mechanism of WZYD from the novel perspective of SANs. Centered on N-WZYDs, this study was conducted at three levels. First, at the material level, we elucidated the formation patterns of N-WZYDs and the roles of the four constituent herbs through systematic de-formulation experiments and nanoscale characterization while analyzing the core structural components of N-WZYDs. Second, at the pharmacodynamic level, we evaluated whether N-WZYDs represent the active form responsible for WZYD's efficacy against CM. Focusing on neuroinflammation and pain signaling pathways, we investigated how N-WZYDs modulate the IL-33/ST2/TRPA1 signaling axis in the brain and used molecular docking to explore correlations between the active components of N-WZYDs and ST2 or TRPA1. Finally, at the intestinal absorption level, we investigated the biodistribution of N-WZYDs, evaluated their uptake and component transport using Caco-2 monolayer cell models, and assessed their effects on 5-HT release from EC cells using RIN-14B cells. By integrating formation patterns, CM-alleviating efficacy, and intestinal absorption profiles of N-WZYDs, we aim to delineate the pathway of decoctions from oral administration to brain efficacy and offer insights into the development of therapeutic natural product-derived nanomedicines.

2. Materials and methods

2.1. Chemicals and reagents

Euodiae Fructus, Ginseng Radix et Rhizoma, Zingiberis Rhizoma Recens, and Jujubae Fructus, authenticated by Prof. Muxin Gong, were obtained from the Anguo Chinese Medicine Market (Hebei, China). Details of these ingredients—including pharmaceutical name, Chinese Pinyin, abbreviation used, full Latin name, and the medicinal part—are listed in Table S1. The standards which included obacunone, rutin, kaempferol-3-*O*-rutinoside, narcissoside, hyperoside, chlorogenic acid, neochlorogenic acid, cryptochlorogenic acid, ginsenoside Rg_1 (Rg_1), and ginsenoside Ro (≥ 98% purity), were purchased from Shanghai Yuanye Biotechnology Co., Ltd. (Shanghai, China); dehydroevodiamine (DeEv), evodiamine (Ev), evocarpine, dihydroevocarpine, 6-gingerol (6-Gi), ginsenoside Re, ginsenoside Rb_1, ginsenoside Rf (≥ 98% purity), rutecarpine (≥ 99.7% purity), and limonin (≥ 99% purity) were purchased from Chengdu Push Biotechnology Co., Ltd. (Chengdu, China); rutaevin (Rv) (≥ 98% purity) was purchased from Absin Bioscience Inc. (Shanghai, China); 6-*O*-*trans*-caffeoylgluconic acid (89.95% purity) was purchased from Chengdu DeSiTe Biological Technology Co. Ltd. (Chengdu, China). Sumatriptan succinate (≥ 98% purity) was purchased from Macklin Biochemical Technology Co., Ltd. (Shanghai, China). Reserpine was purchased from Chengdu Herbpurify Co. Ltd. (Chengdu, China). Chlorpromazine hydrochloride, indomethacin, methyl-β-cyclodextrin, and amiloride hydrochloride (≥ 98% purity) were purchased from Merck KGaA (Darmstadt, Germany).

Inflammation soup (IS) contained 2 $mmol \cdot L^{-1}$ histamine (> 97%) and 2 $mmol \cdot L^{-1}$ serotonin hydrochloride (≥ 98%) (Sigma-Aldrich, St. Louis, MO, USA), 0.2 $mmol \cdot L^{-1}$ prostaglandin (≥ 98%) (Yeasen, Shanghai, China), and 2 $mmol \cdot L^{-1}$ bradykinin (≥ 98%) (Aladdin, Shanghai, China). All compounds were dissolved in HEPES (≥ 99%, Solarbio, Beijing, China).

2.2. Cells and animals

Caco-2 and RIN-14B cell lines were obtained from the Meisen Chinese Tissue Culture Collections (Zhejiang, China). Caco-2 cells were cultured in Dulbecco's modified Eagle's medium (Gibco), and RIN-14B cells were cultured in RPMI 1640 medium. All basic media were supplemented with 10% fetal bovine serum (Gibco) and 1% penicillin/streptomycin (Corning). Cells were cultured at 37 °C with 5% CO_2.

Male Sprague–Dawley rats (200 ± 20 g) and ICR mice (18–22 g) were purchased from Beijing Vital River Laboratory Animal Technology Co., Ltd. (Beijing, China). Animals were housed under standard environmental conditions (a 12-h cycle with light and dark intervals, 22–24 °C) in specific pathogen-free facilities with ad libitum access to food and water. All experimental procedures complied with the Guide for the Care and Use of Laboratory Animals and were approved by the Animal Ethics Committee of Capital Medical University (Authorization No. AEEI-2020-002, AEEI-2020-162).

2.3. Preparation of WZYD, N-WZYDs and S-WZYD

WZYD was prepared as follows: 69 g of Euodiae Fructus, 82.8 g of Zingiberis Rhizoma Recens, 41.4 g of Ginseng Radix et Rhizoma, and 36 g of Jujubae Fructus were soaked in 1400 mL of distilled water for 30 min and then decocted until the volume was reduced to 400 mL. The decoction was finally filtered through gauze to obtain WZYD, with occasional stirring during decoction. Based on reported methods [22], N-WZYDs were isolated from WZYD *via* differential centrifugation coupled with dialysis. First, WZYD was centrifuged sequentially at 3000, 6000 and 10 000 × *g* (30 min each). The resulting supernatant was dialyzed for 12 h against distilled water (MWCO = 3500 Da), replacing the external water every 2 h. The retained dialysate was collected as N-WZYDs, all centrifuged sediments were pooled as S-WZYD. WZYD, N-WZYDs, and S-WZYD were frozen at −80 °C for at least 4 h, lyophilized, and stored in a desiccator. All samples were prepared in sufficient quantities and homogenized for subsequent research.

2.4. Characterization of N-WZYDs

N-WZYDs were irradiated vertically with a light beam to observe Tyndall scattering. The morphology of N-WZYDs was characterized by transmission electron microscopy (TEM; JEM-2100F,

JEOL, Japan) and scanning electron microscopy (SEM; S-4800, Hitachi, Japan). Size distribution, zeta potential, and polydispersity index (PDI) of N-WZYDs were measured by dynamic light scattering (DLS; Brookhaven 90Plus, USA). Particle concentration in N-WZYDs was measured using nanoparticle tracking analysis (NTA; Particle Metrix, Germany). N-WYZDs were suspended in water (10 mg·mL^{-1}) and incubated at 60 °C for 30 min before testing.

Fourier transform infrared (FTIR) spectroscopy was performed using a Nicolet iS5 spectrometer (Thermo Fisher Scientific, USA) equipped with a diamond attenuated total reflectance accessory. Spectra were acquired across the mid-infrared region (4000–400 cm^{-1}) at 4 cm^{-1} resolution. The spectrum of N-WZYDs was compared with those of WZYD and S-WZYD. Widely targeted metabolomics analysis of N-WZYDs was performed by ultra-performance liquid chromatography-tandem mass spectrometry (UPLC-MS/MS). N-WZYDs powder (50 mg) was extracted with 70% methanol (1.2 mL), vortexed (30 s pulses at 30-min intervals × 6), and then centrifuged (12 000 r·min^{-1}, 3 min). The supernatant was filtered (0.22 μm) for UPLC-MS/MS analysis. An Agilent SB-C_{18} column (2.1 mm × 100 mm, 1.8 μm) was used for separation on an ExionLC™ AD UPLC system (SCIEX, Framingham, MA, USA) coupled to a TripleTOF® 6600 mass spectrometer (SCIEX), with detection in both positive and negative ion modes. Components were identified and quantified using the Metware database (Metware, Wuhan, China) and processed with Analyst 1.6.3 software (SCIEX).

2.5. Preparation and characterization of SANs in herbal combinations of WZYD

SANs from all 14 herbal combinations of WZYD (WZY, RS, SJ, DZ, and their binary and ternary combinations) were prepared following the N-WZYDs isolation protocol. All decoctions used herbal mass ratios identical to the original WZYD formula. The morphologies, size distributions, and zeta potentials of the nanophase solutions were characterized by TEM and DLS.

2.6. Preparation and characterization of ethanol-precipitated fraction (EP) and ethanol-soluble fraction (ES) of N-WZYDs

To investigate the compositional nature of the structural framework of N-WZYDs, ethanol precipitation was performed to separate EP and ES. Briefly, 100 mg of N-WZYDs was homogenized in 100 mL of water (60 °C, 30 min), and then 50 mL of the mixture was adjusted to 75% ethanol (*V/V*) and stored at 4 °C for 12 h. After filtration to separate EP and ES, both fractions were dried and reconstituted to 50 mL with water. Untreated N-WZYDs served as controls. Total polysaccharide and protein contents of EP, ES and N-WZYDs were quantified *via* the phenol-sulfuric acid method and the bicinchoninic acid (BCA) assay (NCM, Jiangsu, China).

Active components of EP, ES, and N-WZYDs were analyzed using UPLC-MS/MS (QTRAP 6500+ , AB Sciex, USA) with a Waters ACQUITY UPLC BEH C_{18} column (2.1 mm × 100 mm, 1.7 μm) according to a previously reported method [22]. The mobile phase consisted of 0.1% (*V/V*) formic acid–water (A) and 0.1% (*V/V*) formic acid–acetonitrile (B). The gradient elution program was as follows: 0–5 min, 5%–16% B; 5–7 min, 16%–20% B; 7–11 min, 20%–30% B; 11–16 min, 30%–40% B; 16–21 min, 40%–60% B; 21–26 min, 60%–80% B; 26–29 min, 80%–100% B; 29–32 min, 100% B; 32–32.5 min, 100%–5% B; and 32.5–36 min, 5% B. Compounds were identified by comparing retention times and ion fragments with standards. Fifty-milliliter aliquots of EP, ES, and N-WZYDs were concentrated, dried, reconstituted in 25 mL of methanol, sonicated for 30 min, and filtered through 0.22 μm membranes prior to analysis.

2.7. Animal experimental design

Sixty rats were randomized into sham, model, sumatriptan (5.83 mg·kg^{-1} once every 3 d), WZYD (20.63 g crude drugs·kg^{-1}·d^{-1}), N-WZYDs (20.63 g crude drugs·kg^{-1}·d^{-1}), and S-WZYD (20.63 g crude drugs·kg^{-1}·d^{-1}) groups. The sham and model groups received vehicle. After one week of adaptation, animals underwent surgery. A cannula was implanted into the skull of each rat for IS or HEPES infusion as described previously [19, 20]. Postoperatively, rats were housed individually and allowed to recover for at least 7 days. The sham group received 10 mmol·L^{-1} HEPES buffer (pH 7.4) infused into the dura *via* the cannula. Other groups received IS (10 μL) infused for at least 5 min. IS was administered once every 3 days to mimic CM, 8 times in 22 days.

After 22 days, all rats were anesthetized. Blood was collected from the external jugular vein within 3 min, mixed with ethylenediaminetetraacetic acid, and centrifuged (3000 r·min^{-1}, 20 min, 4 °C). The supernatant was collected. After euthanasia, brains of six rats per group were harvested immediately. The trigeminal nucleus caudalis (TNC) and brainstem regions were dissected on ice and stored at −80 °C for Western blot (WB) or enzyme-linked immunosorbent assay (ELISA). The remaining four rats per group were transcardially perfused with 200 mL of ice-cold saline and fixed with 4% paraformaldehyde. Brains were postfixed in 4% paraformaldehyde for histomorphological assays.

2.8. Behavioral tests

Prior to HEPES or IS injections, rats underwent the facial withdrawal threshold test and heat-induced tail-flick latency test every 3 days to evaluate mechanical allodynia and thermal hyperalgesia. The rats were acclimated to the apparatus for 30 min before testing. The mechanical pain thresholds were assessed using Von Frey filaments (Aesthesio, USA) applied perpendicularly to the periorbital region, with head retraction or facial rubbing recorded as a positive response. The maximum threshold was set at 26 g. Measurements were repeated three times with 2-min intertrial intervals. The thermal pain thresholds were measured by a tail-light tester (KW-GZY, Nanjing, China). The tail-flick response was evoked by applying radiant heat 4 cm from the tail tip. Withdrawal latency was recorded over three trials with 5-min intertrial intervals and an 8-s maximum exposure limit.

2.9. Molecular docking

Compounds structures were obtained from PubChem (https://pubchem.ncbi.nlm.nih.gov/) and processed using OpenBabel 3.1.1. The three-dimensional structures of ST2 and TRPA1 were obtained from the AlphaFold database (https://alphafold.ebi.ac.uk/). AutoDock 1.5.7 was used to perform molecular docking and calculate binding energies between compounds and proteins. Docking results were visualized using PyMOL 3.1.

2.10. ELISA analysis

TNC and brainstems were homogenized in ice-cold PBS and centrifuged (3000 r·min^{-1}, 20 min, 4 °C). CGRP and 5-HT levels in plasma and TNC were quantified using rat CGRP and 5-HT ELISA kits (Nanjing Jiancheng Int., Nanjing, China). Inositol 1,4,5-trisphosphate (IP_3) and calcium levels in the TNC were measured with ELISA kits (Elabscience, Wuhan, China). TNF-α and IL-1β levels in the plasma and brainstems were measured with ELISA kits (Meimian, China; Elabscience). All procedures followed the manufacturers' protocols.

2.11. Western blotting

Proteins from the TNC were extracted using RIPA lysate

(WB3100, NCM, China) containing protease and phosphatase inhibitors, followed by quantification with a BCA kit. Protein samples were separated on 6%, 7.5%, 10% or 15% SDS-PAGE gels (PG110, PG111, PG112, PG114; EpiZyme, China) and transferred to PVDF membranes (ISEQ00010, Merck Millipore, Ireland). Membranes were blocked with 5% skim milk (T1081; Solarbio, Beijing, China) for 2 h at room temperature and incubated with primary antibodies at 4 °C overnight: anti-CGRP (14959S, 1∶1000, Cell Signaling Technology), anti-IL-33 (ab187060, 1∶1000, Abcam), anti-ST2 (60112-1-Ig, 1∶10 000, Proteintech), anti-ITPR1 (19962-1-AP, 1∶300, Proteintech), tubulin (11224-1-AP, 1∶10 000, Proteintech), anti-TRPA1 (YN3017, 1∶1000, Immunoway), anti-c-Fos (YT0884, 1∶1000, Immunoway), anti-p-PLCγ1 (YP0234, 1∶500, Immunoway), anti-PLCγ1 (YM8406, 1∶5000, Immunoway), anti-β-actin (YM8343, 1∶5000, Immunoway), and anti-GAPDH (60004-lg, 1∶10 000, Proteintech). After washing, the membranes were incubated with species-matched HRP-conjugated secondary antibodies. Protein bands were visualized using an enhanced chemiluminescence kit (P10200, NCM) on a Fusion imaging system (Vilber Lourmat, Germany). Band intensities were quantified with ImageJ 1.5.4 software.

2.12. Immunofluorescence

Postfixed TNC tissues were paraffin-embedded and sectioned coronally at a thickness of 10 μm. Serial sections were incubated overnight at 4 °C with primary antibodies: anti-c-Fos antibody (GB11069, 1∶300, Servicebio, China) and anti-Iba1 antibody (GB15105, 1∶500, Servicebio, China). After being washed with PBS, the sections were incubated with fluorescence-conjugated secondary antibodies (GB21303, 1∶300; GB25301, 1∶400; Servicebio, China), rinsed three times, and incubated with DAPI for 10 min. Fluorescence images were acquired using a panoramic scanner and analyzed with CaseViewer software.

2.13. In vivo biodistribution of N-WZYDs

DiR@N-WZYDs were prepared by incubating N-WZYDs (50 mg·mL^{-1}) with 25 μmol·L^{-1} DiR dye (MedChemExpress, Shanghai, China) at a ratio of 4∶1 (*V*/*V*) for 30 min in the dark, followed by centrifugation (12 000 × *g*, 70 min) to remove unbound dye. The labeled N-WZYDs and free DiR were resuspended in purified water. Mice were randomly divided into free DiR control and DiR@N-WZYDs groups (2.0 mg N-WZYDs·g^{-1}). Before the experiment, all mice were subcutaneously injected with reserpine (1.0 mg·kg^{-1}) daily for 10 days to establish CM models. Subsequently, mice were orally administered DiR@N-WZYDs or free DiR. Biodistribution was assessed using an IVIS spectrum imaging system (PerkinElmer, Boston, USA) at 0.5, 1.5, 5.0, and 10.0 h postadministration. At 5.0 and 10.0 h, organs (heart, liver, spleen, lungs, kidneys, intestines) were excised for *ex vivo* fluorescence imaging.

2.14. Cell proliferation assay

Cell proliferation of Caco-2 and RIN-14B cells was assessed by CCK-8 assay according to the manufacturer's instructions. Caco-2 cells were seeded at 5 × 10^4 cells per well in 100 μL of complete medium and exposed to varying concentrations of N-WZYDs for 24 h. RIN-14B cells were seeded in 96-well plates (1 × 10^5 cells per well in 100 μL) and treated with EP, ES, or N-WZYDs at varying concentrations for 24 h. After treatment, the sample medium was removed, 110 μL of complete medium containing 10% CCK-8 was added and incubated for 1 h (37 °C, 5% CO_2). Absorbance at 450 nm was measured using a microplate reader (SpectraMax iD3, Molecular Devices, USA). The cell viability was calculated according to formula (1):

$$\text{Cell viability}\ (\%) = [(A\text{s} - A\text{b})/(A\text{c} - A\text{b})] \times 100\% \quad (1)$$

*A*s: the absorbance of the experimental group; *A*c: the absorbance of the control group; *A*b: the absorbance of the blank group.

2.15. N-WZYDs uptake in Caco-2 and RIN-14B cells

Coumarin-6 (C6; Solarbio, Beijing, China) was loaded as a fluorescent marker. Briefly, 1 μL of C6 stock solution (2 mg·mL^{-1} in DMSO) was mixed with 2 mL of N-WZYDs (2 mg·mL^{-1}) and vortexed for 10 min to prepare C6-labeled N-WZYDs (C6-N-WZYDs). The C6-N-WZYDs were centrifuged (10 000 × *g*, 4 °C, 70 min), washed twice to remove unbound dye, and resuspended in culture medium for experiments.

Confocal laser scanning microscopy (LAS X, Leica, Germany) was employed to visualize uptake. Caco-2 cells were seeded at 5 × 10^4 cells per dish and RIN-14B cells at 1 × 10^5 cells per dish in glass-bottom confocal dishes and cultured for 24 h. After incubation with C6-N-WZYDs for 1 h, the cells were stained with rhodamine-phalloidin (Solarbio, Beijing, China) and DAPI (Beyotime, Shanghai, China) for 30 min, washed three times with PBS, and imaged.

Flow cytometry was performed to quantify uptake in Caco-2 cells. Cells (1 × 10^5 cells per well) were seeded in 24-well plates and cultured for 24 h. The cells were then exposed to 500 μL of C6-N-WZYDs and incubated for 0.5, 1.0, 2.0, 4.0, 6.0 or 8.0 h. After incubation, cells were washed twice with PBS and lysed with 200 μL of RIPA buffer. The lysate was neutralized with 400 μL of culture medium, centrifuged (1000 × *g*, 5 min), and resuspended in PBS for analysis. Fluorescence intensity of 10^4 cells was measured, and uptake at different time points was analyzed using the mean fluorescence intensity.

To investigate uptake pathways, C6-N-WZYDs internalization was assessed after 1 h pretreatment with chemical endocytosis inhibitors: chlorpromazine hydrochloride (CPZ; 20 μg·mL^{-1}, clathrin inhibition), indomethacin (100 μg·mL^{-1}, caveolae inhibition), methyl-β-cyclodextrin (β-CD; 10 μg·mL^{-1}, lipid raft disruption), and amiloride hydrochloride (amiloride; 40 μg·mL^{-1}, macropinocytosis inhibition). After removing the inhibitors, cells were incubated with C6-N-WZYDs for 1 h. For energy-dependent uptake assessment, parallel experiments were conducted at 4 °C. Cells were washed three times with cold PBS, harvested, and analyzed by flow cytometry.

2.16. Transport of components of N-WZYDs across Caco-2 monolayers

Caco-2 cells, which can form tightly polarized monolayers, were used as an intestinal epithelial model. The cells were seeded on 12-well polycarbonate Transwell® plates (corning; 0.4 μm pore size, 1.12 cm^2 surface area) and cultured for 21 days to form confluent monolayers. The apical (AP) side received 500 μL of Caco-2 cell suspension (1 × 10^5 cells per well), and the basolateral (BL) side was filled with 1500 μL of culture medium. During the first week, the medium was replenished every two days, and thereafter daily until monolayer formation (21 days).

Monolayer integrity was assessed by measuring transepithelial electrical resistance (TEER) *via* a Millicell® ERS-2 voltohmmeter (Millipore, USA) over three consecutive weeks. TEER was calculated according to formula (2):

$$\text{TEER}\ (\Omega \cdot \text{cm}^2) = (R_t - R_0) \times A \quad (2)$$

R_t: resistance value of each well, R_0: resistance value of the blank group, *A*: surface area of the Transwell plate (1.12 cm^2).

The differentiation and maturation of Caco-2 cell membranes were assessed by measuring alkaline phosphatase (ALP) activity at the AP membrane. Using a commercial ALP assay kit (Nanjing Jiancheng, Nanjing, China), ALP activity in both AP and BL sides was measured at days 7, 14, and 21. The AP/BL activity

ratio served as an indicator of cell polarization.

Prior to transport experiments, Caco-2 monolayers were washed three times with Hank's balanced salt solution (Gibco). For transport studies, 0.5 or 1.5 mL of N-WZYDs (2 mg·mL^{-1}) was added to either the AP or BL side, with the opposite chamber receiving 1.5 or 0.5 mL of culture medium. At designed time points (30, 60, 90, 120, and 180 min), 500 μL samples were collected from the BL side and 200 μL from the AP side, with equal volumes of fresh medium replenished. The concentrations of transported components of N-WZYDs were quantified by UPLC-MS/MS. The apparent permeability coefficient (P_{app}) and efflux ratio (ER) were used to evaluate transport mechanisms. The P_{app} values were calculated according to formula (3):

$$P_{app} = (\Delta Q/\Delta t)/(AC_0) \quad (3)$$

ΔQ (μg): cumulative drug transport over Δt; Δt (s): cumulative exposure time; $\Delta Q/\Delta t$ (μg·s^{-1}): cumulative transport rate; A (cm^2): surface area of the polycarbonate membrane; C_0 (μg·mL^{-1}): initial concentration of the components.

The ER was calculated according to formula (4):

$$ER = P_{app}(BL \rightarrow AP)/P_{app}(AP \rightarrow BL) \quad (4)$$

P_{app}(BL→AP): permeability coefficients of N-WZYDs components in the BL→AP direction; P_{app}(AP→BL): permeability coefficients of N-WZYDs components in the AP→BL direction.

To investigate P-glycoprotein (P-gp)-mediated transport, Caco-2 monolayers were pretreated with verapamil (50 μg·mL^{-1}) for 1 h prior to N-WZYDs exposure (2 mg·mL^{-1}). Samples from AP and BL sides were collected at predetermined time points and analyzed by UPLC-MS/MS.

2.17. Determination of 5-HT content in the supernatant of RIN-14B cells

RIN-14B cells (1 × 10^6 cells per well) were seeded in 6-well plates and incubated at 37 °C for 24 h. Cells were divided into four groups: blank, N-WZYDs (1.00 mg·mL^{-1}), EP (1.00 mg·mL^{-1}), and ES (1.00 mg·mL^{-1}). After 24 h incubation with treatments, supernatants were collected and 5-HT levels were measured using a 5-HT ELISA kit (Elabscience) following the manufacturer's protocol.

2.18. Statistical analysis

Statistical analyses were performed using IBM SPSS Statistics 26, with graphical representations generated by GraphPad Prism 9.5. Data are presented as mean ± standard deviation (SD). The pain thresholds among six groups were compared using two-way ANOVA with Holm−Sidak's *post hoc* multiple-comparisons tests after verification of normality and homogeneity of variance. Other multi-group comparisons were performed using one-way ANOVA with Tukey's honest significant difference (HSD) test, and nonparametric or heteroscedastic data were analyzed using Kruskal−Wallis tests with Dunn's multiple comparisons. All tests were two-tailed, with $P < 0.05$ considered statistical significance.

3. Results

3.1. Isolation and characterization of N-WZYDs

N-WZYDs were isolated from WZYD by differential centrifugation combined with dialysis [22]. Differential centrifugation was used to remove microsized particles from the decoction, followed by dialysis to eliminate free components and obtain N-WZYDs, which exhibited a distinct Tyndall effect (Fig. 1A). N-WZYDs appeared as a uniform orange-red dispersion. TEM revealed approximately spherical aggregates with diameters of 200−300 nm (Fig. 1B), consistent with SEM images (Fig. 1C). The average particle size, PDI and zeta potential of N-WZYDs were 233.4 ± 11.4 nm, 0.267 ± 0.019, and −27.86 ± 3.08 mV, respectively, indicating a relatively homogeneous particle population. Zeta potential reflects the strength of electrostatic repulsion or attraction between particles. A higher absolute zeta potential (positive or negative) generally corresponds to greater colloidal stability. The absolute zeta potentials values of N-WZYDs indicated that the colloidal phase was relatively stable. NTA results showed that the particle size of N-WZYDs was mainly distributed around 165.0 nm, with a particle concentration of 1.6 × 10^{11} particles·mL^{-1} (Fig. 1E). The difference in the particle sizes determined by DLS and NTA is likely attributable to their different measurement principles. DLS records a hydrodynamic diameter which incorporates the hydration layer, whereas NTA estimates a core diameter using Brownian motion, giving a result closer to the real particle dimensions.

Infrared spectra revealed that N-WZYDs, S-WZYD, and WZYD exhibited highly similar patterns of absorption, indicating common functional groups and structural motifs (Fig. 1F). The small differences in intensity at the 1200−800 cm^{-1} region (e.g., 1016 cm^{-1}) can indicate small variations in the glycosylation patterns or carbohydrate composition. Extensively targeted metabolomic analysis indicated that N-WZYDs were mainly composed of alkaloids (20.75%), flavonoids (14.29%), terpenoids (14.29%), amino acids and their derivatives (11.22%), phenolic acids (10.03%), and lipids (6.80%) (Fig. 1G).

3.2. Formation patterns of N-WZYDs in relation to the constituent herbs in WZYD

To further explore the mechanisms underlying N-WZYDs formation, we prepared nanoaggregates from different combinations of the constituent herbs of WZYD. This strategy enabled a systematic exploration of how different herbal combinations influence the nanoscale characteristics of the resulting N-WZYDs. Furthermore, we explained the particular contribution of each herb to the formation of N-WZYDs and also, we identified the key herbs that drive the self-assembly of N-WZYDs.

As shown in Fig. 2A, aggregates derived from herbal combinations exhibited composite morphological changes compared to individual herbs. This can be explained by the changes in the matrix environment of the decoction that results in the formation of multiple assembly mechanisms [1]. In single-herb decoctions, TEM analysis revealed SANs of approximately 250 nm in WZYD, similar to N-WZYDs, but no such SANs were observed in RS, SJ, or DZ decoctions. SANs with diameters of 50−100 nm and about 250 nm were observed in RS decoction. Spherical nanoparticles with a diameter of about 100 nm were found in SJ decoction, whereas ultrafine nanoparticles < 10 nm were observed in DZ decoction [24, 25]. In co-decoctions, SANs with particle sizes and morphologies similar to those of the N-WZYDs were observed in WZY-RS, WZY-SJ, WZY-RS-SJ, and WZY-SJ-DZ, suggesting that constituents derived from WZY play a critical role in directing the formation of this specific nanoscale structure, as reflected by their sizes and morphologies. In addition, SANs of 100−200 nm diameter were observed in the RS-SJ co-decoction. When DZ was decocted with a single additional herb, the resulting SANs with particle diameters below 50 nm. In contrast, when DZ was decocted with two or more additional herbs, SANs larger than 50 nm were formed. Aggregates in all DZ-containing decoctions exhibited much larger particle sizes when measured by DLS compared to TEM (except N-WZYDs), (Fig. 2B). This difference can be attributed to the abundant macromolecules in DZ, which create colloidal aggregates and are hard to remove, may affect DLS measurements. As shown in Fig. 2C, most SANs had high values of the ab-

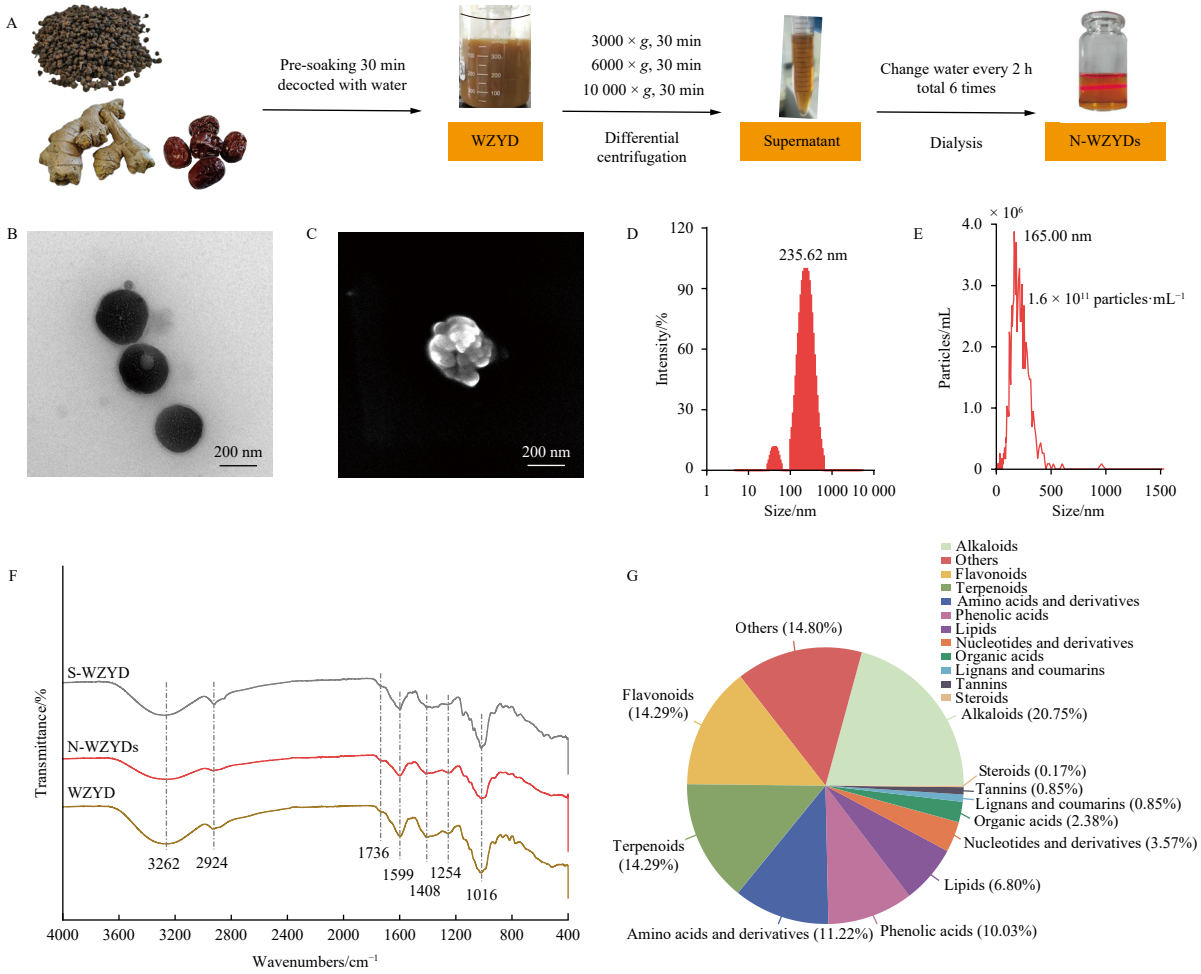


Fig. 1 Preparation process and physicochemical characterization of N-WZYDs. (A) Preparation process and Tyndall effect of N-WZYDs. (B) TEM image and (C) SEM image of N-WZYDs (scale bar, 200 nm). (D) Size distribution of N-WZYDs determined by DLS. (E) Particle concentration of N-WZYDs determined by NTA. (F) Comparison of infrared spectra among N-WZYDs, WZYD, and S-WZYD. (G) Extensively targeted metabolomic profile of N-WZYDs. N-WZYDs: self-assembled nanoaggregates in Wuzhuyu decoction; TEM: transmission electron microscopy; SEM: scanning electron microscopy; DLS: dynamic light scattering; NTA: nanoparticle tracking analysis; WZYD: Wuzhuyu decoction; S-WZYD: centrifuged sediments from Wuzhuyu decoction.

solute zeta potential (> 20 mV), indicating excellent colloidal stability, with the exception of SJ SANs and RS-SJ SANs, which showed lower absolute values of approximately 13 mV.

Eventually, SANs with diameters of 200–300 nm were formed when all four herbs in WZYD were decocted together and allowed to interact. Consistent with the TCM theory, WZY, the sovereign herb in WZYD was confirmed to be indispensable and central to the formation of N-WZYDs. RS and SJ functioned as minister herbs to modulate aggregates size and zeta potential. The addition of DZ as an adjuvant herb significantly fine-tuned the final particle size. N-WZYDs were obtained through the synergistic interactions of all four medicinal ingredients, with stable physicochemical properties and uniform particle sizes.

To identify the constituents of N-WZYDs' scaffold, we investigated the roles of proteoglycans and small molecules in the self-assembly of N-WZYDs. An ethanol precipitation method was used to preliminarily separate the EP and ES from N-WZYDs. TEM images showed that the scaffolds of N-WZYDs were predominantly present in the EP, whereas no aggregates were observed in the ES, indicating that the EP is essential for scaffold formation (Figs. 2D and 2E). ES alone was unable to form aggregate scaffolds under the decocting conditions of WZYD. Interestingly, the scaffolds in the EP were approximately 200 nm in diameter, which was smaller than those in N-WZYDs. This size difference may be attributed to the detachment and subsequent dissolution of most small molecules into the ethanol phase. The BCA assay, phenol sulfate method, and UPLC-MS/MS were used to determine the levels of total protein, polysaccharide, and small molecules in N-WZYDs. EP consisted mainly of macromolecules, such as proteins and polysaccharides, with few small molecules. In contrast, ES was rich in active small molecules, including CA, Rv, and DeEv, but contained only minimal amounts of proteins and polysaccharides (Figs. 2F, 2G and Table S2).

3.3. N-WZYDs attenuated nociceptive behavior in IS-induced CM rats

IS (10 μL) was given every 3 days to induce migraine-like head-scratching behavior (Fig. 3A). The facial periorbital mechanical threshold and tail-flick latency were measured before IS injections to evaluate nociceptive behavior. All groups exhibited a similar pattern of steady weight gain (Fig. 3B). From the fourth infusion of IS (Day 10), the model group showed significantly lower facial periorbital withdrawal thresholds than the sham group (two-way ANOVA, $P < 0.001$). In contrast, there were no significant differences among the sumatriptan, WZYD, N-WZYDs, S-WZYD, and sham group (Fig. 3C). For tail-flick latency, there were no significant differences among the six groups until the fifth IS infusion (Day 13). After the fifth infusion, the model group showed a significant reduction in tail-flick latency compared with the sham group. Tail-flick latencies were significantly longer in the sumatriptan, WZYD, N-WZYDs, and S-WZYD groups than in the model group (Fig. 3D). Overall, N-WZYDs treatment attenuated pain sensitivity in IS-induced migraine, with effects compar-

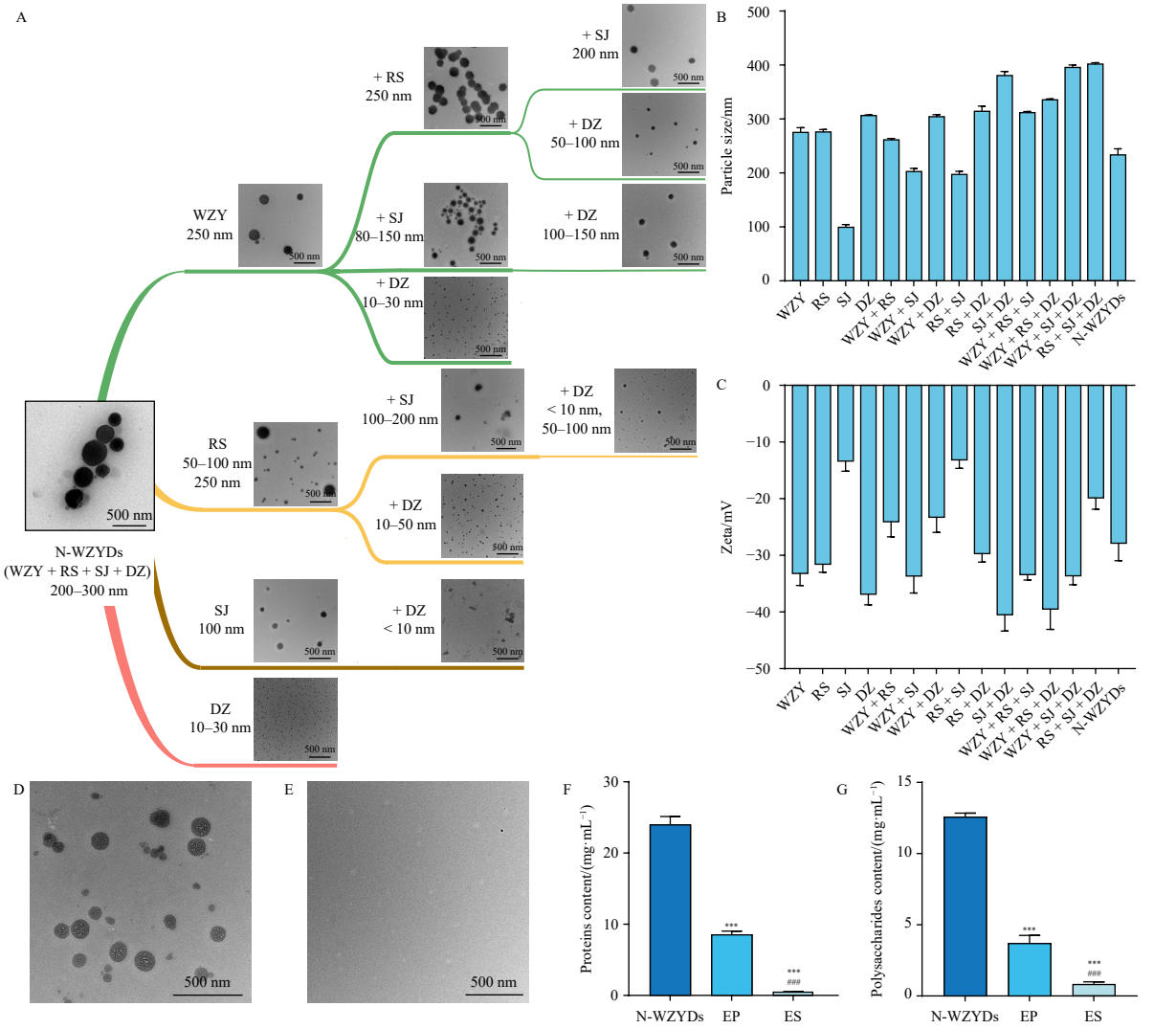


Fig. 2 Formation patterns of N-WZYDs. (A–C) TEM images (scale bar, 500 nm), particle sizes, and zeta potentials of nanoaggregates isolated from the constituent herbs of WZYD. (D) TEM images of EP and (E) ES (scale bar, 500 nm). (F) Protein content and (G) polysaccharide content of N-WZYDs, EP, and ES. ES: ethanol-soluble fraction; EP: ethanol-precipitated fraction. Data are presented as mean ± SD (n = 3). Multi-group comparisons were performed using one-way ANOVA followed by Tukey's honest significant difference (HSD) test. All tests were two-sided. $^{***}P < 0.001$ *vs* N-WZYDs group; $^{###}P < 0.001$ *vs* EP group.

able to those of the positive control and WZYD groups. Thus, N-WZYDs may have therapeutic potential comparable to that of WZYD for treating migraine by reducing pain sensitivity.

3.4. N-WZYDs increased plasma 5-HT and downregulated CGRP in plasma and the TNC in IS-induced CM rats

ELISA results revealed a significant decline in plasma 5-HT levels in the model group compared with the sham group, which was significantly reversed by treatment with sumatriptan, WZYD, N-WZYDs, and S-WZYD (Fig. 3E). However, there were no significant differences in 5-HT expression in the TNC among the sham, model, and N-WZYDs groups. Compared with the model group, TNC 5-HT levels was significantly elevated in the WZYD group, but significantly decreased in the S-WZYD group (Fig. 3F). S-WZYD exerted an adverse effect on the ability of WZYD to increase 5-HT levels in the TNC.

CGRP, a widely recognized migraine-related mediator, is involved in central sensitization within the TNC. CGRP levels in the model group were significantly elevated in both plasma and the TNC compared with the sham group, but were significantly reduced in the sumatriptan, WZYD, and N-WZYDs groups compared with the model group. However, S-WZYD reduced CGRP levels only in plasma. Compared with the model group, there was no significant difference in TNC CGRP levels in the S-WZYD group (Figs. 3G and 3H). WB results further confirmed these findings. Compared with the sham group, TNC CGRP levels were significantly elevated in the model group. Sumatriptan, WZYD, and N-WZYDs all reduced TNC CGRP levels in CM rats, with the N-WZYDs group exhibiting the greatest reduction. There was no significant difference in TNC CGRP levels between the S-WZYD and model groups (Fig. 3I).

3.5. N-WZYDs attenuated neurogenic inflammation and reduced trigeminal system activation in the TNC of IS-induced CM rats

c-Fos serves as a key marker of neuronal activation and is commonly associated with the transmission of pain signals. Immunofluorescence staining was performed to detect c-Fos-positive cells in the TNC. The relative density of c-Fos was significantly higher in the model group than in the sham group. Compared with the model group, the sumatriptan, WZYD, N-WZYDs, and S-WZYD groups showed significantly reduced c-Fos expression. There was no significant difference in c-Fos expression among the N-WZYDs, WZYD, and S-WZYD groups (Figs. 4A and 4B). These findings were further confirmed by WB results, which also showed a marked deregulation of c-Fos expression in the TNC after N-WZYDs treatment compared with the model group (Figs. 4C and 4D).

Iba1 is a marker of microglial activation. Immunofluores-

cence staining revealed that IS significantly increased Iba1 expression in the TNC, whereas N-WZYDs administration reduced Iba1 expression. Compared with N-WZYDs, S-WZYD produced a weaker reduction in Iba1 expression (Figs. 4E and 4F). To evaluate the antineuroinflammatory effects of N-WZYDs in CM rats, we examined the expression of IL-1β and TNF-α in the brainstem. Compared with the sham group, TNF-α and IL-1β expression in the brainstem and plasma was upregulated after repeated IS stimulation and was attenuated by treatment with sumatriptan and WZYD. The neurogenic inflammation in CM rats was significantly reduced by N-WZYDs. Moreover, N-WZYDs showed better effect as compared to S-WZYD in reducing inflammation (Figs. 4G–4J). Overall, N-WZYDs showed more pronounced reductions in these neuronal activation and inflammatory indices than S-WZYD.

3.6. N-WZYDs ameliorated CM by modulating the IL-33/ST2/TRPA1 signaling pathway

To investigate the interactions between the active components of N-WZYDs and the IL-33/ST2/TRPA1 pathway, we performed molecular docking of 22 quantified components of N-WZYDs with ST2 receptor and TRPA1 ion channel, which resulted in 44 docking complexes (Fig. 5A). Binding energies lower than −5.0 kcal·mol^{-1} indicated favorable binding, while values below −7.0 kcal·mol^{-1} suggested strong binding. Among the 44 complexes, binding energies were between −9.2 and −5.6 kcal·mol^{-1}, indicating that all these active compounds exhibited notable binding affinity to both ST2 and TRPA1. Specifically, limonin, Rv, and obacunone formed hydrogen bonds with ST2 residues including ARG-204, SER-126, SER-30, and TRP-31. Meanwhile, narcissoside, limonin, and rutin formed hydrogen bonds with TRPA1 residues including GLN-794, LYS-992, LEU-851, MET-981, ARG-855, LYS-871, ASN-808, ASN-988, and LYS-790. Hydrogen bond formation enhances intermolecular interactions, and increases stability of the component–protein complexes. Components forming such bonds are likely possess higher bioactivity because they can bind more stably to target sites and exert pharmacological effects more effectively. The bioactivity of N-WZYDs could be due to the synergistic actions of multiple components targeting different pathway nodes. It has been previously reported that ginsenosides and ginger extracts can suppress IL-33 expression [26-28]. Consistent with these findings, our docking results suggest that components such as limonin, Rv, and narcissoside in N-WZYDs potentially interact with ST2 or TRPA1, supporting a multi-target mechanism behind the activity of this formula.

Protein expression of IL-33, ST2, and TRPA1 in TNC tissues was highly elevated in CM rats after IS stimulation compared with the sham group, but were markedly downregulated by WZYD, N-WZYDs, and S-WZYD treatment (Figs. 5D–5G). We then investigated the possible molecular pathways connecting IL-33 with TRPA1. WB and ELISA results showed that the p-PLCγ/PLCγ ratio and expression of the inositol 1,4,5-trisphosphate receptor (IP_3R), as well as levels of inositol IP_3 and calcium, were significantly increased in the model group. Treatment with WZYD, N-WZYDs, or S-WZYD markedly attenuated these elevations compared to the model group, with N-WZYDs recapitulating the efficacy of the original decoction (Figs. 5H–5L). No significant difference in IP_3R protein expression was observed between the S-WZYD and WZYD groups. These results suggest that N-WZYDs downregulate TRPA1 expression and alleviate pain by modulating the IL-33/ST2/TRPA1 signaling pathway and the PLCγ-mediated signaling axis linking IL-33 to TRPA1.

3.7. In vivo imaging showed N-WZYDs primarily distributed in the intestinal tract of the mice

To investigate the distribution of N-WZYDs, we conducted *in vivo* imaging studies. N-WZYDs were labeled with DiR, a near-infrared fluorescent dye (excitation: 745 nm, emission: 800 nm). It has been proven that N-WZYDs contain lipophilic substances. As a lipophilic near-infrared fluorescent anthocyanin dye, DiR's two 18-carbon chains can insert into cell membranes or bind to lipophilic biomolecules, facilitating specific and stable staining. Mice were orally administered free DiR or DiR@N-WZYDs, and fluorescence was measured at 0.5, 1.5, 5.0, and 10.0 h post-administration. The fluorescence of DiR@N-WZYDs peaked at 1.5 h, weakened at 5.0 h, and was nearly undetectable at 10.0 h (Fig. 6A). This indicated that DiR@N-WZYDs were metabolized within 10.0 h. We then investigated the *in vivo* biodistribution of N-WZYDs. N-WZYDs primarily concentrated in the intestinal tract of the mice, with no significant fluorescence observed in other organs (Figs. 6B and 6C). Therefore, N-WZYDs are inferred to exert their effects or undergo decomposition mainly within the intestine.

3.8. C6-N-WZYDs uptake in Caco-2 cells peaked at 1 h with major pathways involving macropinocytosis and clathrin-mediated endocytosis

Differentiated Caco-2 cells serve as a mature human intestinal mucosal model. *In vitro*, these cells differentiate into brush border and basolateral membranes, expressing various enzymes and nutrient transporters [29]. To investigate N-WZYDs uptake by Caco-2 cells and elucidate the underlying mechanisms, we examined the intracellular localization and time-dependent uptake kinetics of C6-N-WZYDs in this cell line. Fig. 6E illustrated Caco-2 cell viability remained above 95% at N-WZYD concentrations ranging from 10 to 2000 μg·mL^{-1}, whereas at 3000 μg·mL^{-1} viability was approximately 88.65%. Generally, a sample can be deemed as non-toxic to cells when their survival rate is above 90% [30]. Consequently, N-WZYDs at 2000 μg·mL^{-1} were selected for subsequent investigations. Fig. 6D showed that C6-N-WZYDs were internalized by Caco-2 cells, aggregating around the nucleus. The fluorescence intensity of internalized C6-N-WZYDs in Caco-2 cells peaked at 1 h and gradually decreased after 2 h (Fig. 6F).

To investigate energy-dependent uptake mechanisms, the cellular uptake of C6-N-WZYDs was compared at 4 and 37 °C. Additionally, the cellular uptake mechanisms of C6-N-WZYDs were investigated using specific endocytosis pathway inhibitors. Cells were pretreated with CPZ, indomethacin, β-CD, or amiloride to inhibit clathrin-mediated endocytosis, caveolae-mediated endocytosis, lipid raft-mediated endocytosis, and macropinocytosis, respectively. Flow cytometry results (Fig. 6G) revealed that incubation at 4 °C, which limits cell metabolism and decreases membrane fluidity, led to an approximately 32% decrease in the uptake of C6-N-WZYDs, supporting energy-dependent uptake mechanisms. The residual uptake at 4 °C was likely due to limited active transport or passive diffusion. The cellular uptake of C6-N-WZYDs was not affected by treatment with indomethacin or β-CD. However, amiloride and CPZ significantly decreased the uptake of C6-N-WZYDs by 40%–50%, suggesting that macropinocytosis and clathrin-mediated endocytosis are the predominant uptake pathways. This study showed that N-WZYDs could be intactly internalized by the intestinal cells and clarified their cellular uptake mechanisms.

3.9. Transport of N-WZYDs components across Caco-2 monolayers

Caco-2 cells spontaneously differentiate into tightly connected monolayers that structurally and functionally resemble intestinal epithelium, widely used for *in vitro* oral drug absorption studies [31]. Above results showed that, within a specific concentration range, N-WZYDs exhibited no detectable cytotoxicity in Caco-2 cells and could be internalized (Fig. 6). This suggested that the components of N-WZYDs might be transported across of Caco-2

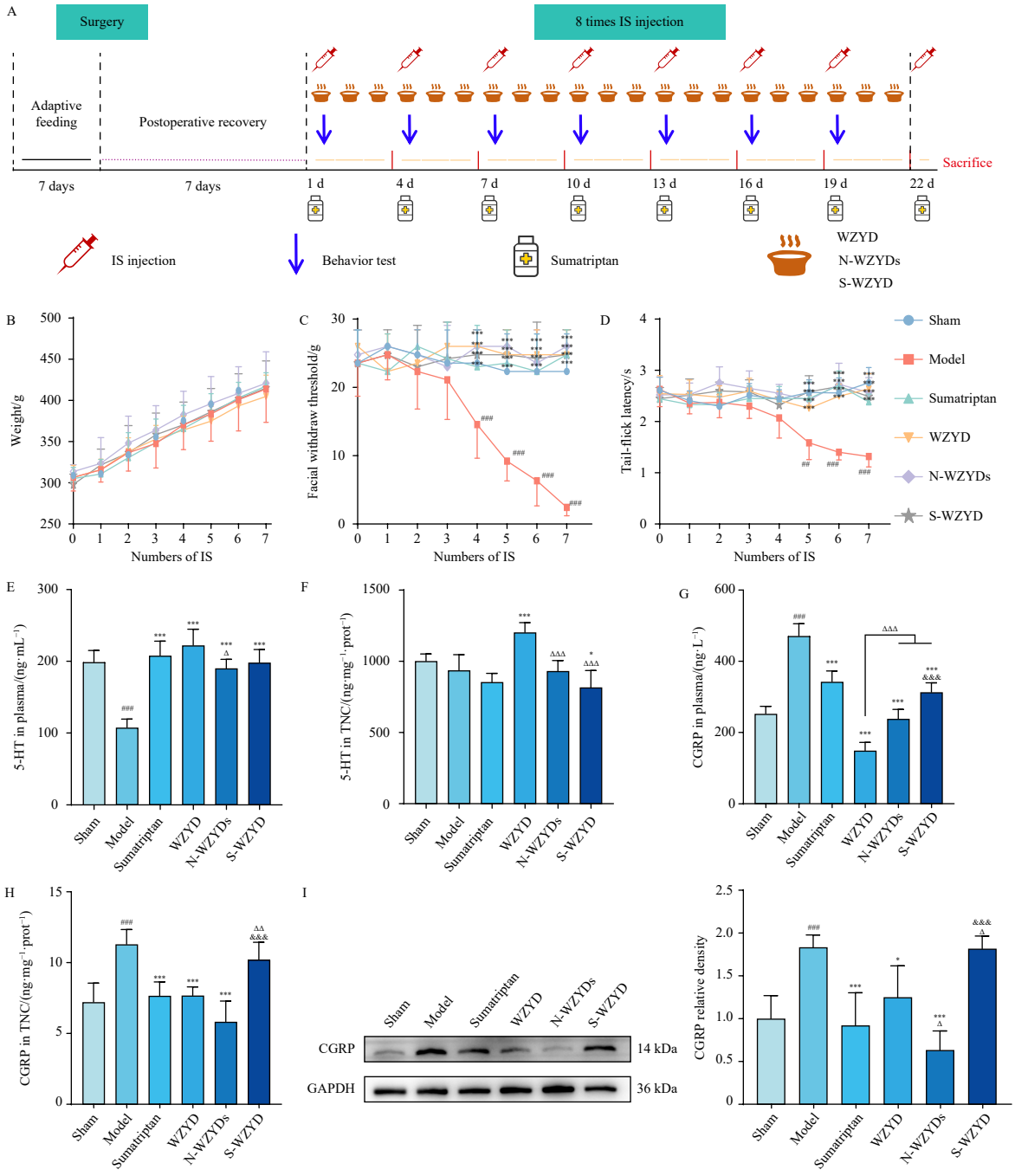


Fig. 3 Evaluation of the effects of WZYD, N-WZYDs, and S-WZYD on IS-induced CM rats. (A) Schematic of model induction and N-WZYDs intervention. Behavioral indices were assessed every 3 days, including (B) weight change, (C) facial mechanical withdrawal threshold, and (D) tail-flick latency (n = 9). (E) Plasma 5-HT content (n = 6). (F) TNC 5-HT content (n = 6). (G) Plasma CGRP content (n = 6). (H) TNC CGRP content (n = 6). (I) Western blot analysis of CGRP levels in the TNC of CM rats (n = 5). IS: inflammation soup; CM: chronic migraine; TNC: trigeminal nucleus caudalis; 5-HT: serotonin; CGRP: calcitonin gene-related peptide. Data are presented as mean ± SD. Pain threshold comparisons among the six groups were analyzed by two-way ANOVA with Holm–Sidak's *post hoc* multiple-comparisons tests. Multi-group comparisons were performed using one-way ANOVA followed by Tukey's HSD test. All tests were two-sided. $^{###}P < 0.001$ *vs* sham group; $^{*}P < 0.05$, $^{***}P < 0.001$ *vs* model group; $^{\Delta}P < 0.05$, $^{\Delta\Delta}P < 0.01$, $^{\Delta\Delta\Delta}P < 0.001$ *vs* WZYD group; $^{\&\&\&}P < 0.001$ *vs* N-WZYDs group.

cells. Therefore, to investigate the absorption of N-WZYDs in the gastrointestinal tract and identify components transportable by Caco-2 cells, we studied the transcellular delivery of N-WZYDs across Caco-2 monolayers.

Caco-2 cells were cultured on polycarbonate filter membranes. Monolayer integrity was verified *via* TEER ≥ 500 Ω·cm^2 [32]. After 21 days of culture, TEER values were 525 ± 19 Ω·cm^2, indicating dense monolayer formation (Fig. 7A). ALP, a brush border marker enzyme, demonstrated progressive differentiation during monolayer maturation. By day 21, the AP/BL ALP activity ratio reached approximately 4, exceeding the threshold of 2 and verifying the establishment of polarized cell morphology and functional brush border formation (Fig. 7B). The integrity of the Caco-2 cell monolayers was further assessed by measuring the apparent permeability coefficient (P_{app}) of fluorescein sodium. The measured mean P_{app} value of 0.77 × 10^{-7} cm·s^{-1} was significantly lower than 1 × 10^{-6} cm·s^{-1}, confirming that the monolayers were sufficiently tight for permeability studies [33,34].

The Caco-2 monolayers were then used to study the bidirectional transport of the components of N-WZYDs across the intestinal epithelium within 180 min. The P_{app} values and transport quantities of Ev, DeEv, Rv, 6-Gi, and Rg_1 are summarized in Table S3. Other components are not discussed, as they were either not transported or were below the detection limit. The P_{app} of sub-

stances across Caco-2 cell monolayers is strongly related to their *in vivo* absorption, effectively reflecting their intestinal absorption capacity [35]. P_{app} values < 1×10^{-6} cm·s^{-1} indicate poor uptake; values between 1×10^{-6} and 10×10^{-6} cm·s^{-1} indicate moderate uptake; and values > 1×10^{-5} cm·s^{-1} indicate high uptake [36]. Ev and 6-Gi showed moderate uptake, with P_{app} values between 1×10^{-6} and 10×10^{-6} cm·s^{-1} during AP→BL transport. DeEv, Rv and Rg_1 had P_{app} values < 1×10^{-6} cm·s^{-1}, indicating poor uptake. ER determines the transport pathway of a substance in the Caco-2 cell monolayer model. An ER < 1.5 indicates passive diffusion, whereas an ER > 1.5 suggests active transport involving transporter proteins [23]. Rg_1 exhibited an ER < 1.5, suggesting that passive diffusion is its primary transport mechanism. Conversely, Ev, DeEv, Rv, and 6-Gi showed an ER > 1.5, indicating their high like-

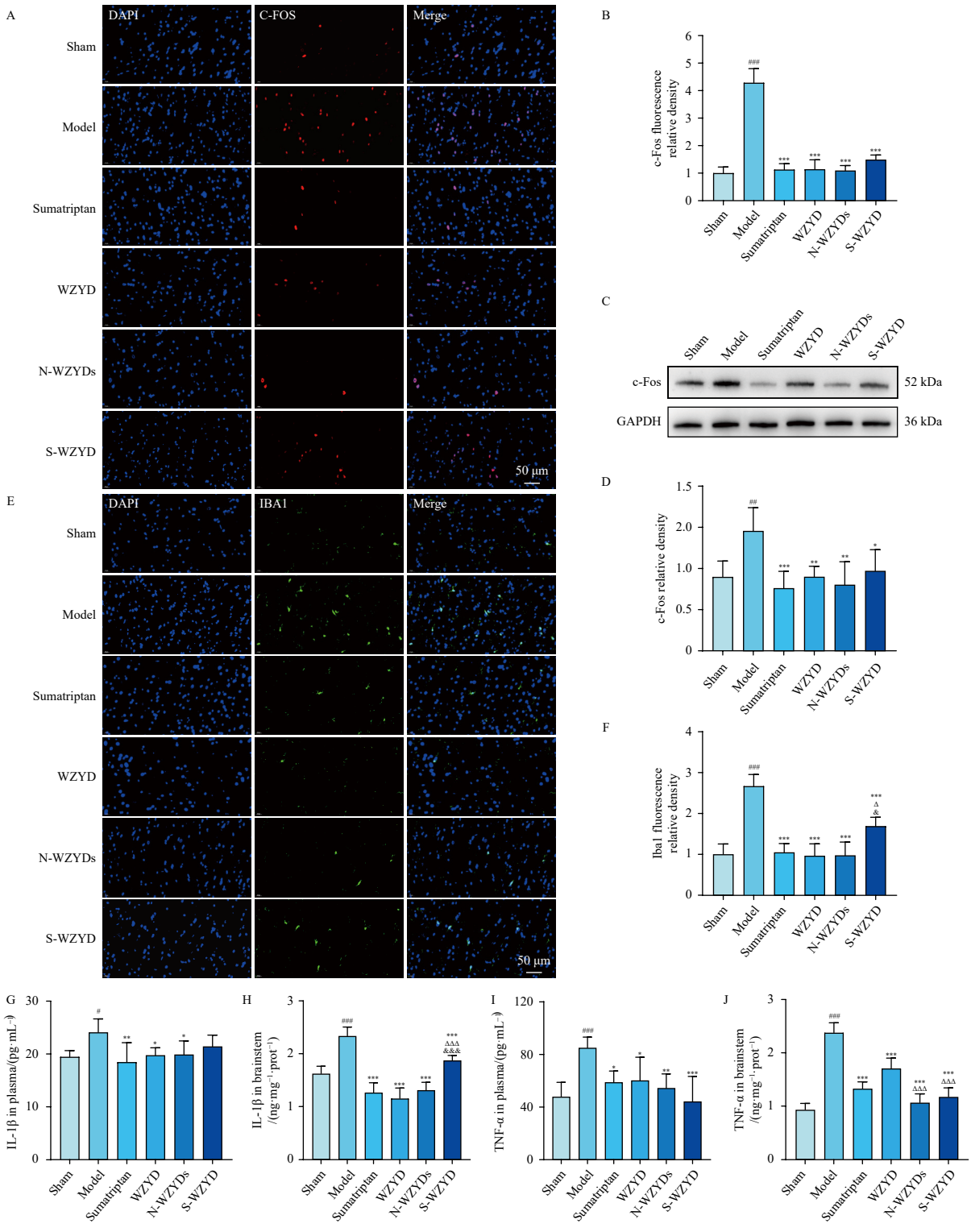


Fig. 4 Effects of WZYD, N-WZYDs, and S-WZYD on trigeminal system activation and neurogenic inflammation. (A) Immunofluorescence images and (B) relative fluorescence density of c-Fos in the TNC (n = 4). (C) Representative Western blots and (D) relative c-Fos expression in the TNC (n = 5). (E) Immunofluorescence images and (F) relative fluorescence density of Iba1 in the TNC (n = 4). (G) Plasma IL-1β content (n = 6). (H) Brainstem IL-1β content (n = 6). (I) Plasma TNF-α content (n = 6). (J) Brainstem TNF-α content (n = 6). Data are presented as mean ± SD. Multi-group comparisons were performed using one-way ANOVA followed by Tukey's HSD test. All tests were two-sided. $^{\#}P < 0.05$, $^{\#\#}P < 0.01$, $^{\#\#\#}P < 0.001$ *vs* sham group; $^{*}P < 0.05$, $^{**}P < 0.01$, $^{***}P < 0.001$ *vs* model group; $^{\Delta}P < 0.05$, $^{\Delta\Delta\Delta}P < 0.001$ *vs* WZYD group; $^{\&}P < 0.05$, $^{\&\&\&}P < 0.001$ *vs* N-WZYDs group.

lihood as substrates for active efflux transporters (Figs. 7C–7G). The critical role of P-gp was further confirmed by a significant reduction in the ER values of all five compounds (Ev, DeEv, Rv, 6-Gi, and Rg_1) when coincubated with verapamil, a P-gp inhibitor (Figs. 7H–7L). In summary, the permeability of these five compounds was determined by both passive diffusion and active efflux. Rg_1 demonstrated passive diffusion with poor uptake. DeEv and Rv experienced both poor passive uptake and active efflux. Ev and 6-Gi exhibited moderate uptake but were limited by efflux.

3.10. N-WZYDs potently stimulated 5-HT release from RIN-14B cells, outperforming individual active components

Given the limited absorption of components within N-WZYDs and previous findings that WZYD acts on EC cells to promote peripheral 5-HT synthesis [19], we utilized RIN-14B cells, an estab-

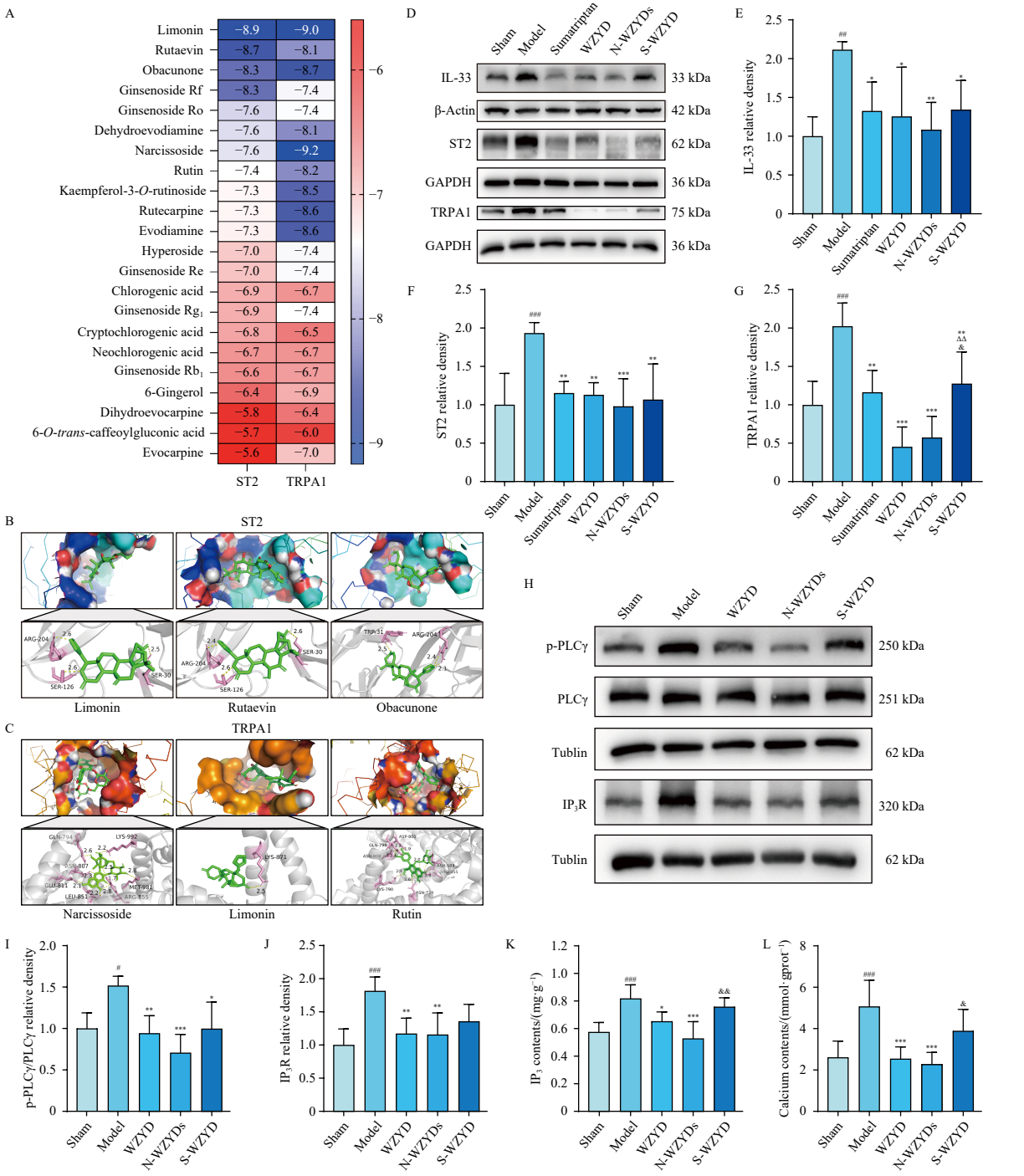


Fig. 5 Effects of WZYD, N-WZYDs, and S-WZYD on the IL-33/ST2/TRPA1 and PLCγ/IP_3/IP_3R signaling axis in CM rats. (A) Heatmap of binding energies (kcal·mol^{-1}) from molecular docking of 22 active components with the ST2 receptor and TRPA1 ion channel. (B and C) Docking results of the top three components with the lowest binding energies and hydrogen bond interactions with the (B) ST2 receptor and (C) TRPA1 ion channel amino acid residues. Active site residues were shown as pink stick models, and active components as green stick models. Yellow dotted lines represented hydrogen bonds interactions. (D) Representative images of IL-33, ST2 and TRPA1 WB results in the TNC (n = 5). (E–G) Quantification of IL-33, ST2, and TRPA1 protein expression. (H) Representative images of p-PLCγ, PLCγ and IP_3R WB results in the TNC (n = 5). (I and J) Quantification of the p-PLCγ/PLCγ ratio and IP_3R protein expression. (K and L) IP_3 and calcium levels in the TNC measured by ELISA (n = 6). IL-33: interleukin-33; ST2: suppression of tumorigenicity 2; TRPA1: transient receptor potential ankyrin 1; PLCγ: phospholipase C gamma; IP_3: inositol 1,4,5-trisphosphate; IP_3R: inositol 1,4,5-trisphosphate receptor. Data are presented as mean ± SD. Multi-group comparisons were performed using one-way ANOVA followed by Tukey's HSD test. All tests were two-sided. $^{\#}P < 0.05$, $^{\#\#}P < 0.01$, $^{\#\#\#}P < 0.001$ *vs* sham group; $^{*}P < 0.05$, $^{**}P < 0.01$, $^{***}P < 0.001$ *vs* model group; $^{\Delta\Delta}P < 0.01$ *vs* WZYD group; $^{\&}P < 0.05$, $^{\&\&}P < 0.01$ *vs* N-WZYDs group.

lished EC cell model, to investigate whether N-WZYDs could promote 5-HT release and the role of their nanostructure. CCK-8 assays were performed to evaluate the cytotoxicity of N-WZYDs, ES, and EP in RIN-14B cells. Figs. 8A–8C illustrated the viability of RIN-14B cells treated with various concentrations of N-WZYDs, ES, and EP. Concentrations of 1.00 mg·mL^{-1} (normalized to the mass of N-WZYDs) for N-WZYDs, ES, and EP, which did not affect cell viability, were selected for subsequent investigations. As shown in Fig. 8D, C6-N-WZYDs could be internalized by RIN-14B cells. N-WZYDs, ES, or EP were added to RIN-14B cells for 24 h to assess their impacts on 5-HT release. Both N-WZYDs and ES had a significant role in promoting 5-HT release by RIN-14B cells compared to the control group. Nevertheless, the amount of 5-HT released by RIN-14B cells in the presence of EP was not significantly different from the amount released by cells in the control group (Fig. 8E). The promotion of 5-HT release by N-WZYDs was also significantly better compared to the effect of the combination of EP and ES, which proves that the structure of N-WZYDs is a key to their success.

4. Discussion

WZYD is a traditional herbal preparation that has therapeutic effects on migraine, nausea, vomiting, and insomnia due to the synergistic effects of its multiple bioactive components and related pathways [20,37,38]. A past study identified 110 components in WZYD by LC-MS [20]. However, solely relying on chemical composition to determine the pharmacological basis of WZYD presents limitations. The specific bioactive constituents of WZYD, the mechanisms and modes of action following oral administration is not fully understood. SANs in decoctions provide a new angle to study TCM deeply, and may explain the mysteries of how classic-

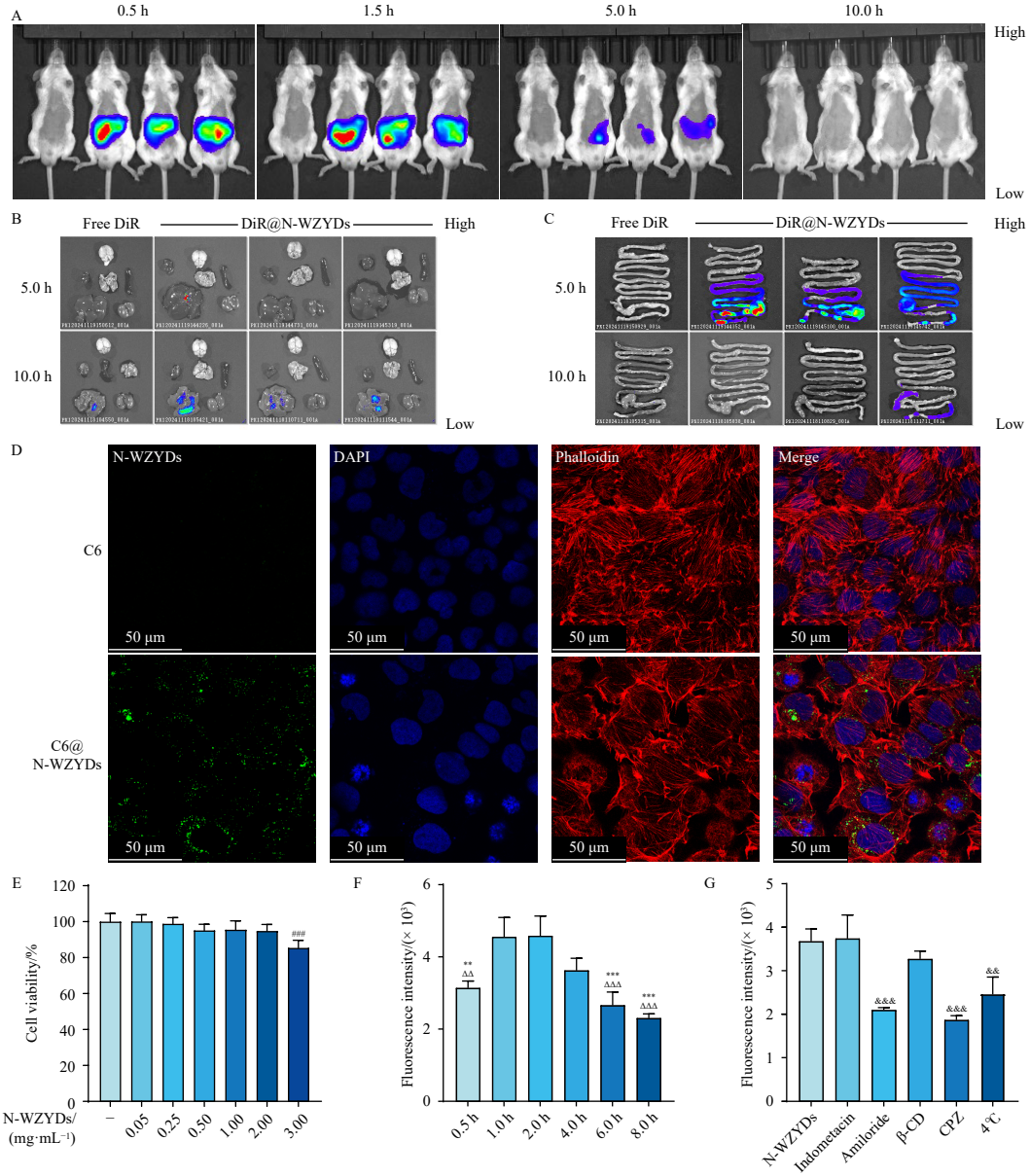


Fig. 6 *In vivo* imaging and Caco-2 cell internalization of N-WZYDs. (A) *In vivo* fluorescence images of CM mice at 0.5, 1.5, 5.0, and 10.0 h after oral administration of free DiR or DiR@N-WZYDs (DiR was preloaded at 5 μmol·L^{-1} in each group, followed by removal of unbound dye; N-WZYDs: 2000 mg·kg^{-1}). (B and C) Fluorescence images of isolated organs from CM mice at 5.0 and 10.0 h after oral administration of free DiR or DiR@N-WZYDs. (D) Uptake and intracellular localization of C6-N-WZYDs in Caco-2 cells at 1.0 h. (E) Caco-2 cell viability after treatment with varying concentrations of N-WZYDs (n = 6). (F) Uptake of C6-N-WZYDs by Caco-2 cells at different time points (0.5, 1.0, 2.0, 4.0, 6.0, and 8.0 h; n = 3). (G) Effects of endocytic inhibitors and temperature on the cellular uptake of C6-N-WZYDs (n = 3). C6-N-WZYDs: coumarin 6-labeled N-WZYDs; β-CD: methyl-β-cyclodextrin; CPZ: chlorpromazine hydrochloride; Amiloride: amiloride hydrochloride. Data are presented as mean ± SD. Multi-group comparisons were performed using one-way ANOVA followed by Tukey's HSD test. All tests were two-sided. $^{###}P < 0.001$ *vs* control group; $^{**}P < 0.01$, $^{***}P < 0.001$ *vs* 1.0 h group; $^{ΔΔ}P < 0.01$, $^{ΔΔΔ}P < 0.001$ *vs* 2.0 h group; $^{&&}P < 0.01$, $^{&&&}P < 0.001$ *vs* N-WZYDs group.

al formulas work. We have obtained pharmacologically active, porous spherical nanoaggregates of WZYD. The N-WZYDs had a size of 200–300 nm, allowing them to penetrate the intestinal mucus barrier (pore size: 100–500 nm) [39]. This characteristic diameter of the particles enables them to avoid rapid clearance and prolongs their contact time with the intestinal epithelium, as evidenced by *in vivo* imaging [40].

Recent studies of carrier-free nanomedicine largely focus on the interactions and self-assembly of small active molecules, and pay little attention to the formula compatibility and the key role of macromolecules in the formation and functionality of nanoaggregates. We have found that the formation of N-WZYDs is in strong agreement with the principle of WZYD composition: sovereign-minister-assistant-courier. As the sovereign herb, WZY alone is capable of generating a core nanoaggregate scaffold, while companion herbs modulate particle size and surface charge. Thus, constituents of WZY seem to be central structural agents, guiding the formation of nanoaggregates with similar key physical features. This inference is made depending on the observed similarities in size and morphology. However, compositional differences, variations in intermolecular interactions, or nanoscale structural differences among aggregates formed in different herb combinations remain possible and require additional high-resolution fractionation and chemical profiling to verify. N-WZYDs consist of EP and ES. EP served as the structural scaffold, which was composed mainly of the macromolecules like proteins and polysaccharides. ES contained active small molecules, such as CA, Rv, and DeEv. Macromolecules are essential for forming N-WZYDs nanostructures, whereas small molecules alone fail to do so. 5-HT is a key neurotransmitter in pain regulation, and the decrease of 5-HT levels may trigger migraine attacks [41]. The proteoglycan-based scaffolds of N-WZYDs enhanced the 5-HT release effect of the encapsulated active components on RIN-14B cells, suggesting that polysaccharides and proteins might not only be carrier components but actively modulate biological activities, which could enhance the effect of active components.

Further investigation into the composition of these macromolecular aggregates, and especially their effect on the absorption and activities of active components should be considered, with the aim of identifying underlying patterns. For example, ginseng polysaccharides could form stable complexes with ginsenoside Re through hydrogen bonding. These complexes help to shield ginsenoside Re against degradation in the oral and gastric stages, allowing its extensive release and absorption in the intestinal digestion stage. Without this protection, most of the ginsenoside Re would be digested and absorbed prematurely in the intestine [42]. Ginseng proteins could encapsulate ginsenoside Re to improve its bioavailability. The protein shell keeps the encapsulated saponins intact during the stomach stage and ensures that they arrive at the small intestine with a desirable slow-release property [43].

TEM images and unimodal particle size distributions are indicative together that N-WZYDs constitute the predominant and apparently homogeneous nanostructures in WZYD. Future studies will use high-resolution separations and fraction-specific chemical profiling, such as asymmetric flow field–flow fractionation (AF4) coupled with UPLC-MS, to separate size fractions and compare their chemical fingerprints to obtain more conclusive evidence of the compositional homogeneity of the derivatized SANs.

WZYD is a classical formula to treat migraine [44]. Repeated dural IS stimulation successfully induced CM, replicating the key features of recurrent migraine, including elevated CGRP and trigeminovascular activation [45]. N-WZYDs exhibited efficacy superior to S-WZYD and comparable to the WZYD group, significantly inhibiting the expression of CGRP (in the plasma and brain), IL-1β, TNF-α, Iba1, TRPA1, and calcium levels in the brains of CM

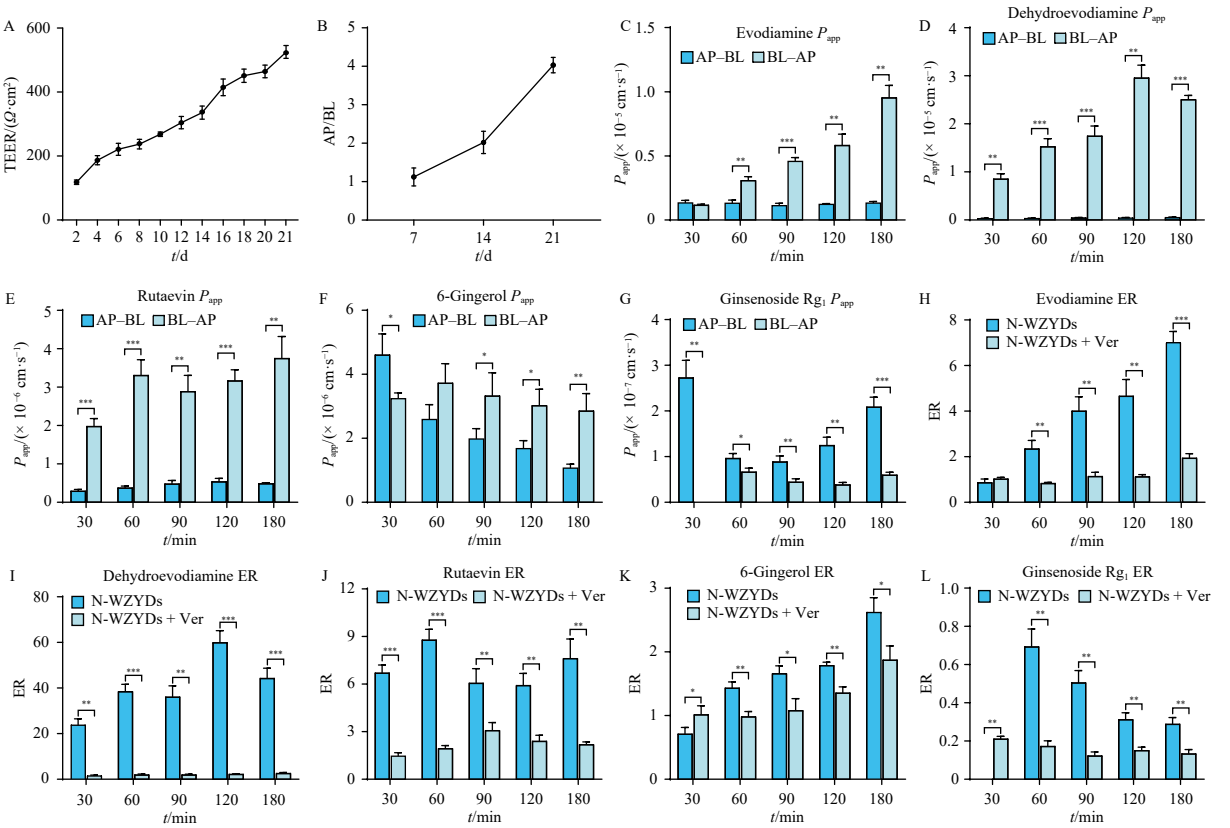


Fig. 7 Establishment of Caco-2 monolayers and transport of N-WZYDs components. (A and B) TEER values (n = 9) and alkaline phosphatase activity (n = 3) of the Caco-2 cell model during monolayer development. (C–G) P_{app} values of evodiamine, dehydroevodiamine, rutaevin, 6-gingerol, and ginsenoside Rg_1 across Caco-2 monolayers (n = 3). Comparisons were made between AP–BL and BL–AP transport at each time point. (H–L) ER of evodiamine, dehydroevodiamine, rutaevin, 6-gingerol, and ginsenoside Rg_1 in Caco-2 monolayers (n = 3). TEER: transepithelial electrical resistance; AP: apical; BL: basolateral; ER: efflux ratio; P_{app}: apparent permeability coefficient; Ver: verapamil. Data are presented as mean ± SD. Statistical significance was determined by an unpaired (two-tailed) Student's t-tests. $^{*}P < 0.05$, $^{**}P < 0.01$, $^{***}P < 0.001$. Comparisons were made between the N-WZYDs and N-WZYDs + verapamil treatment groups at each time point.

rats, confirming that N-WZYDs represent the pharmacologically active form responsible for the WZYD. A limitation of the present study is that there is no depletion–reconstitution experiment (e.g., dialysate or reconstituted fractions) and hence it cannot be assured that WZYD's efficacy is reduced in the absence of N-WZYDs. Even though the comparable efficacy of isolated N-WZYDs and whole WZYD point to the importance of the nanoaggregate fraction, we cannot exclude the contribution of soluble dialysate components. A depletion–reconstitution design will be used in future to accurately determine the proportion of effect N-WZYDs make to the overall therapeutic effect.

IL-33 and TRPA1 have important roles in the central nervous system, and are associated with neurological disorders. As a member of the IL-1 cytokine family, IL-33 modulates neuroimmune crosstalk, neuroinflammation, and pain *via* its receptor, ST2 [46]. Activation of the IL-33/ST2 axis can trigger acute pain and maintain chronic inflammatory pain [47, 48]. TRPA1 is an oxidative stress sensor and is involved in the cause of orofacial neuropathic pain. TRPA1 could promote the release of neuropeptides such as CGRP upon activation. This, in turn, facilitates neurogenic inflammation and sensitizes nociceptors [49-52]. ST2 shares structural homology with Toll-like receptor 4 in its intracellular Toll/IL-1 receptor domain, which may lead to the activation of PLCγ. In trigeminal ganglion neurons, IL-33 can functionally activate TRPA1 by eliciting Ca^{2+} influx driven by PLCγ-mediated increases in intracellular Ca^{2+} [53, 54]. Given the superior regulatory effects of N-WYZDs on CM-related indicators, we further investigated how N-WZYDs modulate the relevant intracerebral pathways implicated in CM pathogenesis based on available literature. We discovered that N-WZYDs suppressed the expression of IL-33, ST2, and TRPA1 in the TNC of CM rats. Moreover, N-WZYDs significantly attenuated the PLCγ signaling pathway, as indicated by lower p-PLCγ/PLCγ ratio and reduced levels of IP_3, IP_3R protein, and calcium. These results suggest that N-WZYDs alleviate CM potentially through inhibition of the IL-33/ST2/TRPA1 pathway (Fig. 9). Molecular docking revealed that components in N-WZYDs (e.g., limonin, Rv, narcissoside, rutin) have low binding energies and are capable of forming hydrogen bonds with key residues of ST2 or TRPA1. However, *in vivo* target engagement is required in future to have more definitive evidence and obtain a definite conclusion.

After confirming that N-WZYDs can be internalized intact by Caco-2 cells, we conducted transport experiments using a Caco-2 monolayer model to explore the absorption behavior of their constituent compounds. Rg_1 presented a low P_{app} ($< 1 \times 10^{-6}$ cm·s^{-1}) and an ER < 1.5 in the Caco-2 transport experiment, showing that it is transported mainly by passive diffusion. The fact that it has a poor permeability is probably explained by its large molecular size and glycosylated structure that hinders its membrane penetration. Its low bioavailability is primarily attributable to poor absorption and not active extrusion, by the fact that there was no significant efflux of it. Rg_1 is extensively metabolized in the intestine, yielding 20(*S*)-protopanaxatriol *via* ginsenosides Rh_1 and F_1, and both the parent compound and its metabolites exhibit significant anti-inflammatory effects [55]. DeEv and Rv exhibited very low intrinsic permeability ($P_{app} < 1 \times 10^{-6}$ cm·s^{-1}) and significant efflux (ER > 1.5), resulting in poor oral bioavailability. Their absorption appears to be hindered by both inefficient membrane penetration and active efflux mechanisms. Ev and 6-Gi displayed moderate permeability and significant efflux activity (ER > 1.5). These findings suggest that although these compounds are capable of entering enterocytes, a substantial portion is pumped back into the lumen by efflux transporters such as P-gp.

Xu et al. reported that the intestinal absorption of Ev and Rv in WZYD was inversely correlated with the overall therapeutic effectiveness in mitigating migraines in rats [56]. Specifically, higher absorption of these compounds was associated with reduced efficacy. The dosage of WZY in classical formulas was higher than that used in modern practice. It is precisely the intestinal excretory mechanisms of its components that mitigates WZY's inherent mild toxicity [57]. Yang et al. reported that 6-Gi stimulates 5-HT secretion from RIN-14B cells [58]. Moreover, 6-Gi is rapidly metabolized in the gut and cleared from the plasma, exhibiting a short terminal half-life of only 7.23 min in rats [59]. The strong active ef-

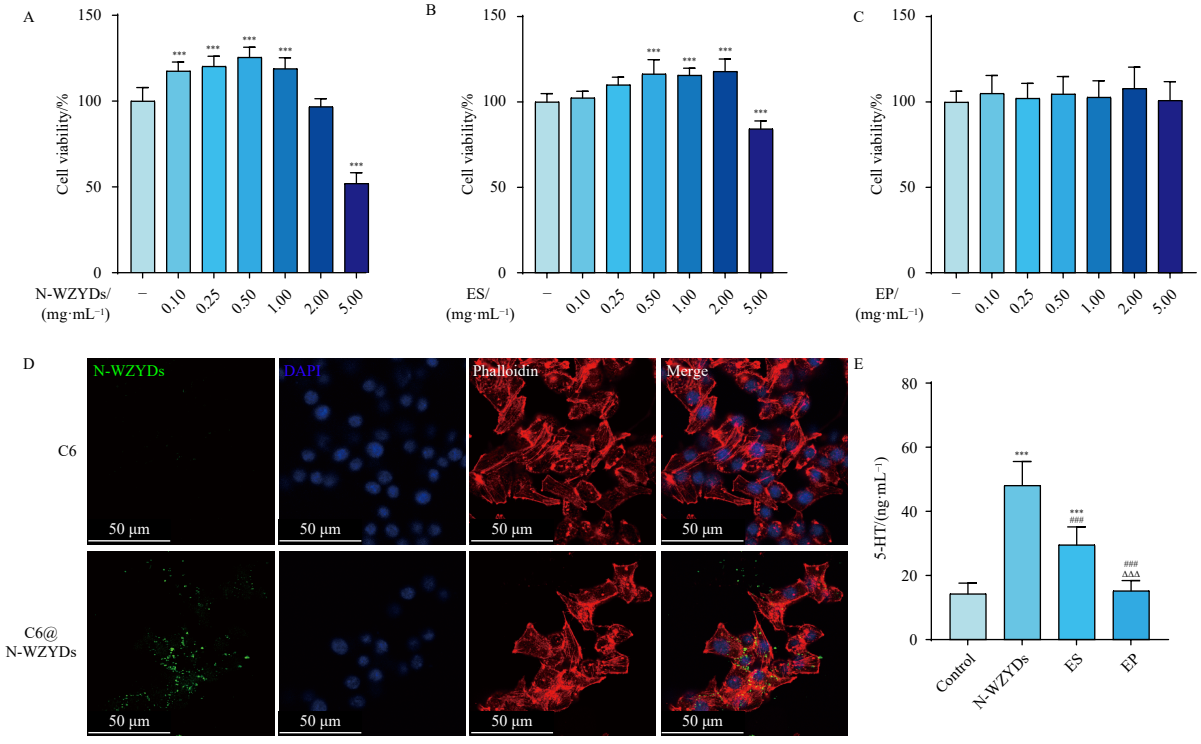


Fig. 8 Effects of N-WZYDs on RIN-14B cells. (A–C) RIN-14B cell viability after treatment with various concentrations of (A) N-WZYDs, (B) ES, and (C) EP ($n = 6$). (D) Uptake and intracellular localization of C6-N-WZYDs in RIN-14B cells at 1.0 h. (E) Effects of N-WZYDs on 5-HT release from RIN-14B cells ($n = 6$). Data are presented as mean ± SD. Multi-group comparisons were performed using one-way ANOVA followed by Tukey's HSD test. All tests were two-sided. $^{***}P < 0.001$ *vs* control group; $^{###}P < 0.001$ *vs* N-WZYDs group; $^{ΔΔΔ}P < 0.001$ *vs* ES group.

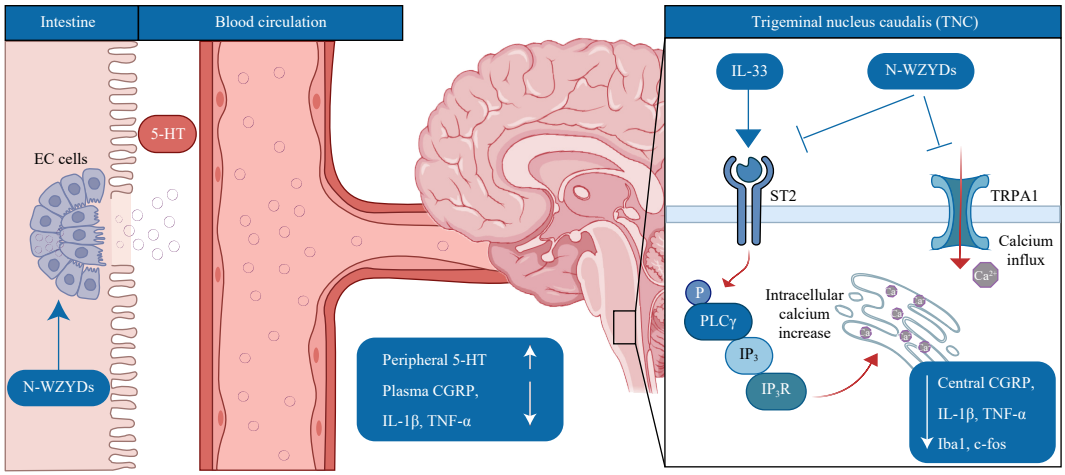


Fig. 9 Schematic illustration of the proposed mechanism of N-WZYDs in CM treatment. N-WZYDs: self-assembled nanoaggregates in Wuzhuyu decoction; CM: chronic migraine; EC: enterochromaffin; 5-HT: serotonin; CGRP: calcitonin gene-related peptide; IL-1β: interleukin-1β; TNF-α: tumor necrosis factor alpha; IL-33: interleukin-33; ST2: suppression of tumorigenicity 2; TRPA1: transient receptor potential ankyrin 1; PLCγ: phospholipase C gamma; IP_3: inositol 1,4,5-trisphosphate; IP_3R: inositol 1,4,5-trisphosphate receptor.

flux of 6-Gi enables it to exert local effects in the intestine or to act through its metabolites formed by the intestinal metabolism. Our findings demonstrate that the compounds loaded in N-WZYDs likely act primarily in the gastrointestinal tract through a mechanism involving poor absorption or enhanced intestinal efflux. This locally stimulated 5-HT release from EC cells, and the increased peripheral 5-HT might act at a distance to suppress neuroinflammatory signaling in the brain by stimulating vagal afferent fibers.

Notably, the trends in peripheral (plasma) and central (TNC) 5-HT levels were divergent: plasma 5-HT was reduced in the CM model and restored by N-WZYDs treatment, whereas TNC 5-HT remained relatively stable across groups. The partial independence of peripheral and central serotonergic pools caused by the blood–brain barrier is probably the cause of this divergence. The apparent stability of TNC 5-HT might be a maladaptive compensatory state which is not adequate to prevent central sensitization but is enough to maintain the baseline level. WZYD restored plasma 5-HT and increased TNC 5-HT, showing a multi-target peripheral–central regulatory role. This indicates that plasma 5-HT may be a biomarker of peripheral pathology and that targeting simultaneously on peripheral and central serotonergic systems may produce better CM therapeutic results.

Ultimately, our study clarified the formation patterns of N-WZYDs and demonstrated their CM-alleviating effects and intestinal absorption characteristics. The scaffold in N-WZYDs, formed by proteoglycans from WZYD, encapsulates active small molecules to exert therapeutic effects. Despite the fact that they only constituted a minor part of WZYD, N-WZYDs showed comparable CM-alleviating effects as the whole decoction. They promoted 5-HT release from EC cells with superior efficacy to that of free active components alone and alleviated hyperalgesia by increasing peripheral 5-HT levels. This highlights the significance of existing forms of bioactive components for therapeutic efficacy and supports rational optimization of WZYD to more concentrated and efficient treatments. The key components of N-WZYDs (Ev, DeEv, Rv, 6-Gi, and Rg_1) may act locally in the intestine to achieve CM therapy. Based on these findings of N-WZYDs, our future studies will focus on mimicking their natural self-assembly strategies to advance the development of novel therapeutic agents and nanodelivery systems for herbal formulations.

5. Conclusion

N-WZYDs represented the principal active form responsible for the pharmacological effects of WZYD and demonstrated CM-relieving efficacy, potentially through inhibition of the IL-33/ST2/TRPA1 pathway. Molecular docking found limonin, Rv, and narcissoside to be high affinity binding to ST2 or TRPA1, indicating that these compounds may be involved in the IL-33/ST2/TRPA1 axis. Concerning herbal formulation, the formation of N-WZYDs relied on the synergistic contributions of all four constituent herbs, with WZY playing the primary role. Compositionally, the formation of N-WZYDs required the involvement of macromolecular scaffolds and small-molecule bioactive constituents. N-WZYDs exhibited intestine-targeted effects through poor absorption or enhanced intestinal efflux of bioactive compounds (Ev, DeEv, Rv, 6-Gi, and Rg_1). In the intestinal environment, intact N-WZYDs potently stimulated 5-HT release from EC cells and increased peripheral 5-HT levels to alleviate CM, demonstrating superior efficacy compared to the active components alone. In conclusion, the SANs in WZYD underlie their efficacy, and their scaffolds are critical for modulating the biological activity of the constituent compounds. This study provides a nanoscale viewpoint to explain the material basis and action mechanisms of TCM formulations.

Funding

This work was supported by the National Key R&D Program of China (No. 2023YFC3504000), the Beijing Natural Science Foundation–Capital Clinical Medicine Innovation Joint Fund (No. L2510038), the National Natural Science Foundation of China (No. 81473360), and the Beijing Pharmaceutical and Health Collaborative Initiative for High-Quality R&D of Traditional Chinese Medicine (No. zyygzl-2025-027).

Supporting information

Supporting information for this work can be obtained by contacting the corresponding authors *via* E-mail.

Declaration of competing interest

These authors have no conflict of interest to declare.

References

1 Xiang JW, Meng Y, Zhao MY, et al. Super-self-assembly extraction from natural herbs. *Nano Res.* 2025;18(2):94907094. https://doi.org/10.26599/NR.2025.94907094.
2 Zhou JW, Zhang J, Gao GZ, et al. Boiling licorice produces self-assembled protein nanoparticles: a novel source of bioactive nanomaterials. *J Agric Food Chem.* 2019;67(33):9354-9361. https://doi.org/10.1021/acs.jafc.9b03208.
3 Wu JJ, Yang Y, Yuan XY, et al. Role of particle aggregates in herbal medicine decoction showing they are not useless: considering *Coptis chinensis* Decoction as an example. *Food Funct.* 2020;11(12):10480-10492. https://doi.org/10.1039/d0fo02179b.

4 Lü SW, Su H, Sun S, et al. Isolation and characterization of nanometre aggregates from a Bai-Hu-Tang Decoction and their antipyretic effect. *Sci Rep*. 2018;8(1):12209. https://doi.org/10.1038/s41598-018-30690-5.
5 Zhou JW, Gao GZ, Chu QP, et al. Chromatographic isolation of nanoparticles from Ma-Xing-Shi-Gan-Tang Decoction and their characterization. *J Ethnopharmacol*. 2014;151(3):1116-1123. https://doi.org/10.1016/j.jep.2013.12.029.
6 Chen M, Wang PL, Li T, et al. Comprehensive analysis of Huanglian Jiedu Decoction: revealing the presence of a self-assembled phytochemical complex in its naturally-occurring precipitate. *J Pharm Biomed Anal*. 2021;195:113820. https://doi.org/10.1016/j.jpba.2020.113820.
7 Zou LJ, Li QL, Hou Y, et al. Self-assembled glycyrrhetinic acid derivatives for functional applications: a review. *Food Funct*. 2022;13(24):12487-12509. https://doi.org/10.1039/d2fo02472a.
8 Dai L, Liu KF, Si CL, et al. Ginsenoside nanoparticle: a new green drug delivery system. *J Mater Chem B*. 2016;4(3):529-538. https://doi.org/10.1039/c5tb02305j.
9 Fan YQ, Liu YQ, Wu Y, et al. Natural polysaccharides based self-assembled nanoparticles for biomedical applications: a review. *Int J Biol Macromol*. 2021;192:1240-1255. https://doi.org/10.1016/j.ijbiomac.2021.10.074.
10 Gao GZ, He CQ, Wang HQ, et al. Polysaccharide nanoparticles from Isatis indigotica Fort. root decoction: diversity, cytotoxicity, and antiviral activity. *Nanomaterials (Basel)*. 2021;12(1):30. https://doi.org/10.3390/nano12010030.
11 Lin D, Lin W, Gao GZ, et al. Purification and characterization of the major protein isolated from Semen Armeniacae Amarum and the properties of its thermally induced nanoparticles. *Int J Biol Macromol*. 2020;159:850-858. https://doi.org/10.1016/j.ijbiomac.2020.05.070.
12 Ma BL, Yin C, Zhang BK, et al. Naturally occurring proteinaceous nanoparticles in Coptidis Rhizoma extract act as concentration-dependent carriers that facilitate berberine absorption. *Sci Rep*. 2016;6:20110. https://doi.org/10.1038/srep20110.
13 Wang YL, Mu Y, Zhang YL, et al. Accessible and effective nanomedicines: self-assembly products from Chinese herbal medicines (CHMs). *Adv Funct Mater*. 2025;35(9):2416151. https://doi.org/10.1002/adfm.202416151.
14 Guo XH, Luo WK, Wu LY, et al. Natural products from herbal medicine self-assemble into advanced bioactive materials. *Adv Sci (Weinh)*. 2024;11(35):e2403388. https://doi.org/10.1002/advs.202403388.
15 Huang XM, Liu XJ, Lin XY, et al. Thermodynamics driving phytochemical self-assembly morphological change and efficacy enhancement originated from single and co-decoction of traditional Chinese medicine. *J Nanobiotechnol*. 2022;20(1):527. https://doi.org/10.1186/s12951-022-01734-w.
16 Burch RC, Buse DC, Lipton RB. Migraine: epidemiology, burden, and comorbidity. *Neurol Clin*. 2019;37(4):631-649. https://doi.org/10.1016/j.ncl.2019.06.001.
17 Santoro A, Fontana A, Copetti M, et al. Real-world insights into the effectiveness and tolerability of onabotulinumtoxin A in chronic migraine: a long-term evaluation of up to 11 years. *Toxins (Basel)*. 2025;17(4):208. https://doi.org/10.3390/toxins17040208.
18 Headache Classification Committee of the International Headache Society (IHS). The international classification of headache disorders, 3rd edition. *Cephalalgia*. 2018;38(1):1-211. https://doi.org/10.1177/0333102417738202.
19 Nan N, Gong MX, Wang Q, et al. Wuzhuyu decoction relieves hyperalgesia by regulating central and peripheral 5-HT in chronic migraine model rats. *Phytomedicine*. 2022;96:153905. https://doi.org/10.1016/j.phymed.2021.153905.
20 Song ZM, Li MJ, Zhou ZW, et al. Wuzhuyu decoction relieves chronic migraine by regulating 5-HT1A and 3A receptors-mediated CREB signaling pathway in brain and intestine. *Pharmaceuticals (Basel)*. 2025;18(3):426. https://doi.org/10.3390/ph18030426.
21 Liu HW, Zou YH, Cao KG, et al. Efficacy of modified Wuzhuyu decoction Granule (MWDG) for migraine patients with cold and stasis obstructing meridian syndrome: a randomized, double-blind, placebo-controlled trial. *Chin J Integr Med*. 2018;24:409-414. https://doi.org/10.1007/s11655-017-2547-5.
22 Wang Q, Li MJ, Guo XM, et al. Differences in components and anti-inflammatory and analgesic activities of two phase states of Wuzhuyu decoction. *Chin J Chin Mater Med*. 2024;49(21):5865-5876. https://doi.org/10.19540/j.cnki.cjcmm.20240719.301.
23 Duan SJ, Zheng H, Tang JR, et al. The transport of polyphenols from *Camellia fascicularis* in Caco-2 cells based on UPLC-ESI-MS/MS. *Food Chem X*. 2025;25:102240. https://doi.org/10.1016/j.fochx.2025.102240.
24 Xu YL, Wang BY, Zhang MM, et al. Carbon dots as a potential therapeutic agent for the treatment of cancer-related anemia. *Adv Mater*. 2022;34(19):e2200905. https://doi.org/10.1002/adma.202200905.
25 Guo XM, Wang Q, Li MJ, et al. Differences in intestinal absorption characteristics of nanophase in single and combined decoctions of Ginseng Radix et Rhizoma and Zingiberis Rhizoma Recens based on everted gut sac model. *Chin J Exp Tradit Med Form*. 2024;30(22):231-242. https://doi.org/10.13422/j.cnki.syfjx.20240962.
26 Long J, Liu XK, Kang ZP, et al. Ginsenoside Rg1 ameliorated experimental colitis by regulating the balance of M1/M2 macrophage polarization and the homeostasis of intestinal flora. *Eur J Pharmacol*. 2022;917:174742. https://doi.org/10.1016/j.ejphar.2022.174742.
27 Wang L, Zhang QQ, Xu YY, et al. Ginsenoside Rb1 Suppresses AOM/DSS-induced colon carcinogenesis. *Anticancer Agents Med Chem*. 2023;23(9):1067-1073. https://doi.org/10.2174/1871520623666230119092735.
28 Jafarzadeh A, Mohammadi-Kordkhayli M, Ahangar-Parvin R, et al. Ginger extracts influence the expression of IL-27 and IL-33 in the central nervous system in experimental autoimmune encephalomyelitis and ameliorates the clinical symptoms of disease. *J Neuroimmunol*. 2014;276(1-2):80-88. https://doi.org/10.1016/j.jneuroim.2014.08.614.
29 Jiao WY, Sang YX, Wang XH, et al. Effects of 6-shogaol on glucose uptake and intestinal barrier integrity in Caco-2 cells. *Foods*. 2023;12(3):503. https://doi.org/10.3390/foods12030503.
30 Song HD, He AJ, Guan X, et al. Fabrication of chitosan-coated epigallocatechin-3-gallate (EGCG)-hordein nanoparticles and their transcellular permeability in Caco-2/HT29 cocultures. *Int J Biol Macromol*. 2022;196:144-150. https://doi.org/10.1016/j.ijbiomac.2021.12.024.
31 Feng L, Xiao X, Liu J, et al. Immunomodulatory effects of *Lycium barbarum* polysaccharide extract and its uptake behaviors at the cellular level. *Molecules*. 2020;25(6):1351. https://doi.org/10.3390/molecules25061351.
32 Sharma S, Tripathi P, Sharma J, et al. Flavonoids modulate tight junction barrier functions in hyperglycemic human intestinal Caco-2 cells. *Nutrition*. 2020;78:110792. https://doi.org/10.1016/j.nut.2020.110792.
33 Chen C, Li T, Chen ZX, et al. Absorption rates and mechanisms of avenanthramides in a Caco-2 cell model and their antioxidant activity during absorption. *J Agric Food Chem*. 2020;68(8):2347-2356. https://doi.org/10.1021/acs.jafc.9b06576.
34 Hubatsch I, Ragnarsson EGE, Artursson P. Determination of drug permeability and prediction of drug absorption in Caco-2 monolayers. *Nat Protoc*. 2007;2(9):2111-2119. https://doi.org/10.1038/nprot.2007.303.
35 Pan HY, Bai M, Zheng WT, et al. Absorption and transport of polysaccharides from soybean seed coat in the Caco-2 cell model and their interaction with the MUC2 protein. *Int J Biol Macromol*. 2025;309(Pt 3):143039. https://doi.org/10.1016/j.ijbiomac.2025.143039.
36 Yee S. *In vitro* permeability across Caco-2 cells (colonic) can predict *in vivo* (small intestinal) absorption in man: fact or myth. *Pharm Res*. 1997;14(6):763-766. https://doi.org/10.1023/a:1012102522787.
37 Xu ZY, Yuan YT, Yuan YM, et al. Safety assessment of Wuzhuyu decoction extract: acute and subacute oral toxicity studies in rats. *Drug Chem Toxicol*. 2024;47(6):889-896. https://doi.org/10.1080/01480545.2024.2309341.
38 Li MJ, Song ZM, Wang KS, et al. Key targets of brain-gut coordination in Wuzhuyu decoction treating chronic migraine based on proteomics. *J Pharm Biomed Anal*. 2025;295:117064. https://doi.org/10.1016/j.jpba.2025.117064.
39 Lai SK, Wang YY, Wirtz D, et al. Micro- and macrorheology of mucus. *Adv Drug Deliv Rev*. 2009;61(2):86-100. https://doi.org/10.1016/j.addr.2008.09.012.
40 des Rieux A, Fievez V, Garinot M, et al. Nanoparticles as potential oral delivery systems of proteins and vaccines: a mechanistic approach. *J Control Release*. 2006;116(1):1-27. https://doi.org/10.1016/j.jconrel.2006.08.013.
41 le Grand SM, Supornsilpchai W, Saengjaroentham C, et al. Serotonin depletion leads to cortical hyperexcitability and trigeminal nociceptive facilitation *via* the nitric oxide pathway. *Headache*. 2011;51(7):1152-1160. https://doi.org/10.1111/j.1526-4610.2011.01931.x.
42 Zhu Y, Yue JH, Yan RY, et al. Enhancement in the intestinal absorption of ginsenoside Re by ginseng polysaccharides and its mechanisms. *Food Chem*. 2025;488:144914. https://doi.org/10.1016/j.foodchem.2025.144914.
43 Sheng YY, Yang WL, Li YX, et al. Preparation of ginsenoside Re-ginseng protein nanoparticles and their *ex vivo* and *in vivo* studies. *Food Biosci*. 2025;71:107196. https://doi.org/10.1016/j.fbio.2025.107196.
44 Xu M, Zhang JY, Shi ZH, et al. Amelioration of nitroglycerin-induced migraine in mice *via* Wuzhuyu decoction: inhibition of the MZF1/PGK1 pathway and activation of NRF2 antioxidant response. *J Ethnopharmacol*. 2024;326:117930. https://doi.org/10.1016/j.jep.2024.117930.
45 Zhang W, Yang YP, Zhang XY, et al. Astragaloside IV relieves central sensitization by regulating astrocytic ROS/NF-κB nuclear translocation signaling in chronic migraine male rats. *Phytother Res*. 2025;39(3):1438-1452. https://doi.org/10.1002/ptr.8436.
46 Liew FY, Girard JP, Turnquist HR. Interleukin-33 in health and disease. *Nat Rev Immunol*. 2016;16(11):676-689. https://doi.org/10.1038/nri.2016.95.
47 Wang LJ, Zhang JY, Qiu SJ, et al. IL-33/ST2 drives inflammatory pain *via* CCL2 signaling and activation of TRPV1 and TRPM8. *Commun Biol*. 2025;8(1):724. https://doi.org/10.1038/s42003-025-08119-3.
48 Li PY, Yu Q, Nie HM, et al. IL-33/ST2 signaling in pain and itch: cellular and molecular mechanisms and therapeutic potentials. *Biomed Pharmacother*. 2023;165:115143. https://doi.org/10.1016/j.biopha.2023.115143.
49 Obata K, Katsura H, Mizushima T, et al. TRPA1 induced in sensory neurons contributes to cold hyperalgesia after inflammation and nerve injury. *J Clin Invest*. 2005;115(9):2393-2401. https://doi.org/10.1172/JCI25437.
50 Souza MAD, Nassini R, Geppetti P, et al. TRPA1 as a therapeutic target for nociceptive pain. *Expert Opin Ther Targets*. 2020;24(10):997-1008. https://doi.org/10.1080/14728222.2020.1815191.
51 Xu RY, Pan YS, Zheng KG, et al. IL-33/ST2 induces macrophage-dependent ROS production and TRPA1 activation that mediate pain-like responses by skin incision in mice. *Theranostics*. 2024;14(13):5281-5302. https://doi.org/10.7150/thno.97856.
52 Iannone LF, Nassini R, Patacchini R, et al. Neuronal and non-neuronal TRPA1 as therapeutic targets for pain and headache relief. *Temperature (Austin)*. 2022;10(1):50-66. https://doi.org/10.1080/23328940.2022.2075218.
53 Chen ZJ, Luo JL, Li J, et al. Interleukin-33 promotes serotonin release from enterochromaffin cells for intestinal homeostasis. *Immunity*. 2021;54(1):151-163.e6. https://doi.org/10.1016/j.immuni.2020.10.014.
54 Ikehata Y, Oshima E, Hayashi Y, et al. Fibroblast-derived IL-33 exacerbates orofacial neuropathic pain *via* the activation of TRPA1 in trigeminal ganglion neurons. *Brain Behav Immun*. 2025;123:982-996. https://doi.org/10.1016/j.bbi.2024.11.003.
55 Lee SY, Jeong JJ, Eun SH, et al. Anti-inflammatory effects of ginsenoside Rg1 and its metabolites ginsenoside Rh1 and 20(*S*)-protopanaxatriol in mice with TNBS-induced colitis. *Eur J Pharmacol*. 2015;762:333-343. https://doi.org/10.1016/j.ejphar.2015.06.011.
56 Xu YS, Qiu F, Wu S, et al. UPLC-MS/MS determination of active components from Wuzhuyu decoction in plasma and brain tissues of nitroglycerin-induced migraine rats. *Chin J Chin Mater Med*. 2020;45(3):645-654. https://doi.org/10.1155/2019/6156754.
57 Wang KS, Li MJ, Song ZM, et al. Investigating the material basis and mechanisms of toxicity reduction in processing and compatibility of Euodiae Fructus based on UPLC-MS/MS quantitative analysis and UHPLC-Q-TOF-MS metabolomics. *Phytochem Anal*. 2025;36(7):1990-2010. https://doi.org/10.1002/pca.70006.
58 Yang MQ, Ye LL, Liu XL, et al. Gingerol activates noxious cold ion channel TRPA1 in gastrointestinal tract. *Chin J Nat Med*. 2016;14(6):434-440. https://doi.org/10.1016/S1875-5364(16)30040-1.
59 Nakazawa T, Ohsawa K. Metabolism of [6]-gingerol in rats. *Life Sci*. 2002;70(18):2165-2175, https://doi.org/10.1016/s0024-3205(01)01551-x.